Exploring the Heliogyro's Superior Orbital Control Capabilities for Solar Sail Halo Orbits

Heiligers, Jeannette; Guerrant, D.; Lawrence, D

DOI
10.2514/1.G002184

Publication date
2017

Published in
Journal of Guidance, Control, and Dynamics: devoted to the technology of dynamics and control

Citation (APA)
Heiligers, J., Guerrant, D., & Lawrence, D. (2017). Exploring the Heliogyro's Superior Orbital Control Capabilities for Solar Sail Halo Orbits. *Journal of Guidance, Control, and Dynamics: devoted to the technology of dynamics and control*, *40*(10), 2569-2586. https://doi.org/10.2514/1.G002184

Exploring the Heliogyro's Orbital Control Capabilities for Solar Sail Halo Orbits

Jeannette Heiligers[1]

Delft University of Technology, Kluyverweg 1, 2629 HS Delft, the Netherlands

Daniel Guerrant[2]

Deep Space Systems Inc, Littleton, CO 80127, USA

Dale Lawrence[3]

University of Colorado, Boulder, CO 80309, USA

Solar sailing is an elegant form of space propulsion that reflects solar photons off a large membrane to produce thrust. Different sail configurations exist, including a traditional fixed polygonal flat (FPF) sail and a heliogyro, which divides the membrane into a number of long, slender blades. The magnitude and direction of the resulting thrust depends on the sail's attitude with respect to the Sun (cone angle). At each cone angle, an FPF sail can only generate force constrained to a particular magnitude and direction, while the heliogyro can arbitrarily reduce the thrust magnitude through the additional control of pitching the blades. This gives the heliogyro more force control authority, which is exploited in this paper for orbital control of solar sail, Sun-Earth, sub-L_1 halo orbits through a linear-quadratic regulator feedback controller. Two test cases are considered, quantifying either the maximum error in the injection state or the maximum delay in solar sail deployment due to

[1] Marie Curie Research Fellow, Faculty of Aerospace Engineering. AIAA Member.
[2] Senior Engineer, Deep Space Systems Inc., 8341 Sangre De Cristo Rd Suite 205, Littleton, CO 80127.
[3] Professor, Aerospace Engineering Sciences, ECAE-197, 429 UCB. Associate Fellow AIAA.

* Part of this work has been presented at the *International Symposium on Space Flight Dynamics* (ISSFD), October 19 – 23, 2015, Munich, Germany

deployment failure at injection from which the nominal orbit can still be recovered. This paper finds that the heliogyro can accommodate approximately an order of magnitude larger injection error than an FPF sail and a significantly larger sail deployment delay of up to 20.2 days in some cases.

Nomenclature

$\mathbf{a}$	=	Solar sail acceleration vector, km/s^2
$\tilde{\mathbf{a}}$	=	Averaged solar sail acceleration vector, km/s^2
A	=	Area, m^2
a_c	=	Solar sail characteristic acceleration, km/s^2
a_{co}	=	Amplitude of the collective blade pitch profile, rad
a_{cy}	=	Amplitude of the cyclic blade pitch profile, rad
a_{hp}	=	Amplitude of the half-p blade pitch profile, rad
F	=	Solar sail force, N/m^2
$\mathbf{K}$	=	Gain matrix
m	=	Mass, kg
$\hat{\mathbf{m}}$	=	Unit normal vector of FPF sail
$\hat{\mathbf{n}}$	=	Unit normal vector of heliogyro blade
N	=	Number of heliogyro blades
P	=	Solar radiation pressure, N/m^2
$\mathbf{r}_C$	=	Dimensionless solar sail position vector in circular restricted three-body problem
$r_\odot$	=	Sun-sail distance, km
r_{AU}	=	Sun-Earth distance, km
$\hat{\mathbf{s}}$	=	Unit Sun-direction vector
$s_{L_i,3}$	=	Third component of the $\hat{\mathbf{s}}_{L_i}$ unit vector
t	=	Dimensionless time

$\mathbf{u}$ = Control vector, rad

U = Dimensionless effective potential

$\mathbf{x}$ = Dimensionless state vector

$\hat{\mathbf{z}}$ = Unit vector perpendicular to the Earth's orbital plane

α = Cone angle of solar sail acceleration vector, rad

β = Solar sail lightness number

γ = Angle between $\hat{\mathbf{p}}$ - and $\hat{\mathbf{d}}_3$ -axes, rad

δ = Clock angle of solar sail acceleration vector, rad

$\delta\mathbf{u}$ = Feedback control vector, rad

$\delta\mathbf{x}$ = Dimensionless state error vector

$\Delta\mathbf{r}_0$ = Dimensionless injection error on position vector

$\Delta\dot{\mathbf{r}}_0$ = Dimensionless injection error on velocity vector

Δt_0 = Dimensionless solar sail deployment delay

ε = Dimensionless error tolerance

η = Angle between $\hat{\mathbf{s}}$ - and $\hat{\mathbf{d}}_1$ -axes, rad

θ = Heliogyro blade pitch angle, rad

λ = Eigenvalue

μ = Mass ratio of the circular restricted three-body problem

$\mu_\odot$ = Gravitational parameter of the Sun, km^3/s^2

$\boldsymbol{\xi}$ = Unstable eigenvector

ϕ_{cy} = Phase angle of the cyclic blade pitch profile, rad

ϕ_{hp} = Phase angle of the half-p blade pitch profile, rad

ψ_i = Heliogyro i^{th} blade azimuth angle, rad

$\boldsymbol{\omega}$ = Dimensionless angular momentum vector of circular restricted three-body problem synodic

reference frame

Ω = Heliogyro spin rate, deg/s

$\boldsymbol{\Omega}$ = Heliogyro spin axis

Subscripts

0 = At time $t = 0$

C = In the synodic circular restricted three-body problem reference frame $C\left(\hat{\mathbf{x}}, \hat{\mathbf{y}}, \hat{\mathbf{z}}\right)$

$C,1$ = Referring to, or with respect to, first primary in circular restricted three-body problem

$C,2$ = Referring to, or with respect to, second primary in circular restricted three-body problem

i = Blade number

l = In $\hat{\mathbf{l}}$-direction of the reference frame $S\left(\hat{\mathbf{s}}, \hat{\mathbf{l}}, \hat{\mathbf{p}}\right)$, N/m^2

L_i = In the i^{th} blade's reference frame $L_i\left(\hat{\mathbf{l}}_1, \hat{\mathbf{l}}_2, \hat{\mathbf{l}}_3\right)$

max = Maximum

min = Minimum

nom = Referring to nominal conditions

p = In $\hat{\mathbf{p}}$-direction of the reference frame $S\left(\hat{\mathbf{s}}, \hat{\mathbf{l}}, \hat{\mathbf{p}}\right)$, N/m^2

pos = In direction of position vector

s = In $\hat{\mathbf{s}}$-direction of the reference frame $S\left(\hat{\mathbf{s}}, \hat{\mathbf{l}}, \hat{\mathbf{p}}\right)$, N/m^2

S = In the Sun reference frame $S\left(\hat{\mathbf{s}}, \hat{\mathbf{l}}, \hat{\mathbf{p}}\right)$

sail = Referring to the main sail

vane = Referring to the solar sail vanes

vel = In direction of velocity vector

I. Introduction

Solar sailing is a relatively new form of spacecraft propulsion that exploits solar radiation pressure by using a large, very thin and highly reflective membrane to reflect solar photons, thereby producing thrust [1, 2]. As a propellant-less form of propulsion, it has great potential for high-energy and long-duration missions and has recently been successfully demonstrated in space with the IKAROS [3], NanoSail-D2 [4] and LightSail-1 missions[4]. Each of these three missions employed a fixed polygonal flat (FPF) solar sail; however, renewed interest exists in the heliogyro concept [5, 6]. This solar sail concept divides the sail area into a number of long, slender blades which are deployed from a central hub and flattened by spin-induced tension [1]. Not only does this allow simple packaging and deployment, it also removes the need for a relatively heavy mechanical deployment and stiffening structure as required for the FPF sail configuration. The heliogyro concept is therefore more efficient, allowing a higher force per unit mass because of a lower sail loading (the spacecraft mass to sail area ratio). Note that in this paper, the FPF sail and the heliogyro are assumed to be manufactured conventionally, namely, consisting of a polymer support onto which a non-photonic reflective metal layer is deposited.

Significant research has been conducted regarding the heliogyro's blade dynamics, stability and control [7] and its attitude control moment authority [8], but much remains to be explored in its orbital dynamics and control capabilities, which appear to have some interesting possibilities. For example, the force vector with respect to the Sun-line that an FPF sail can achieve is constrained to the surface of a "force bubble". A coning strategy can scale down the *average* force magnitude, but only over long periods of time, e.g., at orbital rate [9]. Instead, the heliogyro can scale down the force magnitude in any direction within minutes by pitching its blades, which reduces the heliogyro's effective sail area. The heliogyro can therefore "fill up" the force bubble, allowing finer force control, which is exploited in this paper for orbital control. In particular, the ability to correct for orbit injection errors and delays in solar sail deployment at injection into solar sail, Sun-Earth, sub-L_1 halo orbits is investigated and compared to the performance of an FPF solar sail. Note that the gravitational effect of the Moon on these Sun-Earth, sub-L_1 halo orbits is not considered in this paper.

[4] LightSail | The Planetary Society, http://sail.planetary.org/, accessed 22 April 2016

The heliogyro is expected to outperform the FPF sail in terms of orbit correction capabilities because of the following: the time evolution of the acceleration vector of a solar sail determines how the sailcraft will reach its mission target. To optimize this trajectory for some index, three control variables are available: when considering an FPF sail, two of the control variables include the sail loading (σ , which is a function of the area-to-mass ratio of the solar sail) and the optimized time-dependent direction of the solar sail acceleration vector. However, this optimal profile is a local one, i.e., the one related to the chosen value for σ . Unless the mass of the sailcraft can be varied, a (complicated at present) way to recover the third degree of freedom would be the use of a photonic material deposited on the sail. A simpler way is to vary the sail area and this is where the heliogyro gains advantage through its significant capability to vary the sail area exposed to Sunlight.

A solar sail sub-L_1 halo orbit has been proposed for several mission concepts (e.g., Geostorm [10] and Sunjammer [11]) and is one of the key missions enabled by solar sail technology [12]. This mission concept exploits the solar sail's continuous thrust to efficiently position a platform around the Sun-Earth line, sunward of the L_1 point. From such a vantage point, a platform like Sunjammer can almost double the warning time [11] for solar storms over existing infrastructure at L_1 (e.g., SOHO (ESA/NASA, 1996), ACE (NASA, 1997), WIND (NASA, 2004) and DSCOVR (NOAA/NASA, 2015)). This increased warning time is essential to allow operators of ground and space assets enough time to take appropriate action for incoming solar storms. This mission concept has been investigated quite extensively (e.g., References [10-14]) with Reference [14] showing the sub-L_1 point's controllability by varying the FPF sail's effective area through the use of control vanes. Compared to a heliogyro, this area variation is small, because the entire heliogyro sail area can be considered to be control vanes. Superior orbital control capabilities are therefore once again expected for a heliogyro compared to an FPF solar sail with vanes when considering unavoidable orbit injection errors and potential solar sail deployment difficulties at injection into a solar sail sub-L_1 halo orbit.

This paper evaluates the performance of a heliogyro relative to an FPF sail (with vanes) for the sub-L_1 station keeping application, and is structured as follows. First, Section II explains the heliogyro force model and gives a detailed explanation of the reference frames involved, with details of their transformations given in the Appendix. Section III outlines a range of possible pitch profiles of the heliogyro's blades, followed by the impact of these pitch profiles on the heliogyro's force generating capabilities in Section IV. Section V derives and presents the solar sail halo orbits that serve as a test case throughout this paper, followed by the design of a linear-quadratic regulator

(LQR) to maintain these orbits under injection errors and sail deployment delays in Section VI. The results for injection errors are presented in Section VII.A, while the results for a time delay in solar sail deployment are presented in Section VII.B.

II. Heliogyro force model

Different solar sail force models exist, including the ideal solar sail reflectance model [1, 2], which considers the sail to be perfectly reflecting and perfectly flat, without wrinkles or optical imperfections. Under these assumptions, the incoming solar photons are specularly reflected. The solar radiation pressure force and acceleration then act perpendicular to the local sail surface or the heliogyro blade. References [1, 2] highlight the need to use a more realistic force model, e.g., the one coming from scalar scattering theory (SST), which includes specular reflection, diffuse reflection, and absorption. However, SST does not consider the polarization of light in surface scattering, which is taken into account in the so-called Vector Scattering Theories (VSTs) [15-17], which is beyond the aim of this paper. In the interest of a more transparent exposition of the relative advantages of a heliogyro over an FPF sail, this paper will assume the ideal solar sail reflectance model, taking the realistic value for Sunjammer's lightness number (see below Eq. (8)) as the absolute upper bound in our analyses.

With the assumption of perfect specular reflection, Eq. (1) gives the solar radiation pressure acceleration of the sailcraft due to the i^{th} heliogyro blade, i.e., the fraction of total sailcraft radiation pressure acceleration due to a single blade [1, 18]. The total sailcraft radiation pressure acceleration is then obtained by summing the acceleration in Eq. (1) for all blades.

$$\mathbf{a}_{i,L_i} = 2P\frac{A_i}{m}\cos^2\alpha_i\hat{\mathbf{n}}_{L_i} \tag{1}$$

In Eq. (1), P is the solar radiation pressure at the considered Sun-sailcraft distance (e.g., 4.563×10^{-6} N/m^2 at 1 Astronomical Unit (AU)), A_i is the i^{th} heliogyro blade's area and m is the spacecraft mass. The i^{th} blade's cone angle, α_i, is the cone angle between the Sun direction and the i^{th} blade's normal, $\hat{\mathbf{n}}_{L_i}$, where the subscript L_i refers to the i^{th} blade frame, one of four reference frames used in this work: $S\left(\hat{\mathbf{s}},\hat{\mathbf{l}},\hat{\mathbf{p}}\right)$, $D\left(\hat{\mathbf{d}}_1,\hat{\mathbf{d}}_2,\hat{\mathbf{d}}_3\right)$, $B\left(\hat{\mathbf{b}}_1,\hat{\mathbf{b}}_2,\hat{\mathbf{b}}_3\right)$ and $L_i\left(\hat{\mathbf{l}}_1,\hat{\mathbf{l}}_2,\hat{\mathbf{l}}_3\right)$ [18], see Figure 1, with their transformations detailed in the Appendix:

1. Sun coordinate system, $S\left(\hat{\mathbf{s}},\hat{\mathbf{l}},\hat{\mathbf{p}}\right)$

   - $\hat{\mathbf{s}}$: Sun-spacecraft unit vector
   - $\hat{\mathbf{l}}$: When defining $\hat{\mathbf{z}}$ as the unit vector perpendicular to the Earth's orbital plane, $\hat{\mathbf{l}} = \left(\hat{\mathbf{z}} \times \hat{\mathbf{s}}\right) / \left|\hat{\mathbf{z}} \times \hat{\mathbf{s}}\right|$
   - $\hat{\mathbf{p}}$: Completes the right handed reference frame, $\hat{\mathbf{p}} = \hat{\mathbf{s}} \times \hat{\mathbf{l}}$

2. Despun coordinate system, $D\left(\hat{\mathbf{d}}_1,\hat{\mathbf{d}}_2,\hat{\mathbf{d}}_3\right)$

   - $\hat{\mathbf{d}}_1$: Along the heliogyro spin axis $\boldsymbol{\Omega}$
   - $\hat{\mathbf{d}}_2$: Completes the right handed reference frame (along blade 4 at time $t = 0$ for the 4-bladed heliogyro of Figure 1)
   - $\hat{\mathbf{d}}_3$: Along blade 1 at time $t = 0$, where the orientation of blade 1 at $t = 0$ is defined by the angle γ with respect to $\hat{\mathbf{p}}$

3. Body coordinate system, $B\left(\hat{\mathbf{b}}_1,\hat{\mathbf{b}}_2,\hat{\mathbf{b}}_3\right)$

   - $\hat{\mathbf{b}}_1$: Fixed along blade 1
   - $\hat{\mathbf{b}}_2$: Completes the right handed reference frame (along blade 2 at time $t = 0$ for the 4-bladed heliogyro of Figure 1)
   - $\hat{\mathbf{b}}_3$: Along the heliogyro spin axis $\boldsymbol{\Omega}$

   This reference frame is thus fixed to the heliogyro body and aligned along the centerline of blade 1.

4. i^{th} blade coordinate system, $L_i\left(\hat{\mathbf{l}}_1,\hat{\mathbf{l}}_2,\hat{\mathbf{l}}_3\right)$

   - $\hat{\mathbf{l}}_1$: Along i^{th} blade span
   - $\hat{\mathbf{l}}_2$: Along i^{th} blade chord
   - $\hat{\mathbf{l}}_3$: Normal to i^{th} blade ($\hat{\mathbf{l}}_3 \,||\, \hat{\mathbf{n}}_{L_i}$)

   The blade coordinate systems differs from the body coordinate system $B\left(\hat{\mathbf{b}}_1,\hat{\mathbf{b}}_2,\hat{\mathbf{b}}_3\right)$ because they are aligned along different blade centerlines (for i different from 1), and because the blades are generally

pitched relative to the body frame. Blade motion other than rigid-body pitching is neglected in this paper, but this motion is expected to be small and damp within minutes [7, 19].

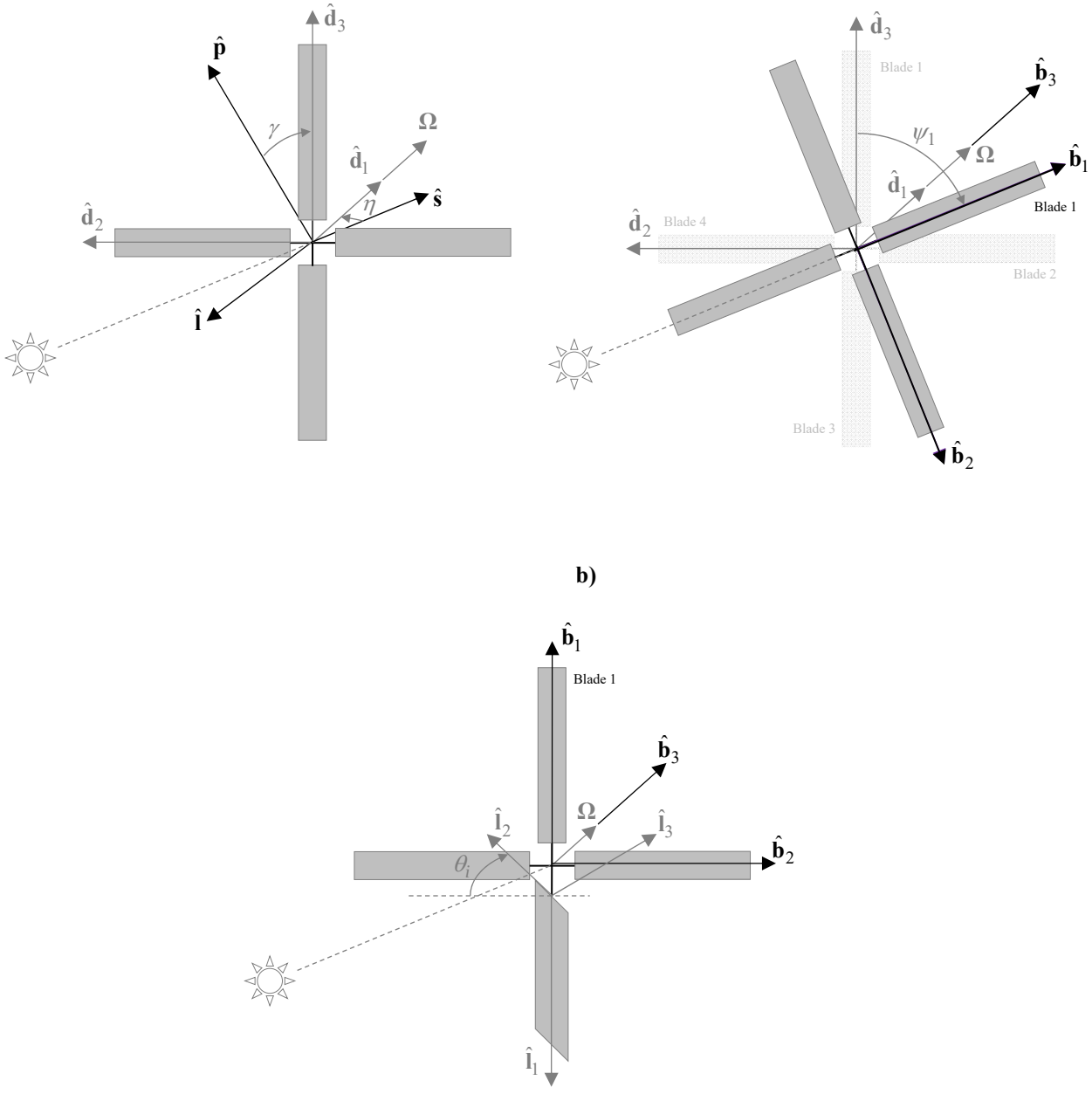

Figure 1 Definition of reference frames. a) S- and D-frames. b) D- and B-frames. c) B- and L_i-frames.

Finally, note that there is a slight difference in the definition of the $D\left(\hat{\mathbf{d}}_1,\hat{\mathbf{d}}_2,\hat{\mathbf{d}}_3\right)$-frame with its definition in Reference [8] as well as in the use of the terms cone and clock angle. While Reference [8] refers to the heliogyro's attitude angles η and γ as cone and clock angles, this paper adopts the definitions as in Reference [1], where the angles α and δ are referred to as cone and clock angles that describe the direction of the solar sail acceleration vector with respect to the Sun coordinate system, $S\left(\hat{\mathbf{s}},\hat{\mathbf{l}},\hat{\mathbf{p}}\right)$, see Figure 2. Note that, for an FPF solar sail, the definitions are almost interchangeable ($\eta=\alpha;\ \gamma=\frac{1}{2}\pi-\delta$), because the direction of the solar sail acceleration vector of an FPF sail is fully defined by its attitude. Instead, for a heliogyro both its attitude (through the angles η and γ) and the blades' cone angles (i.e., α_i) define the direction of the solar sail acceleration vector.

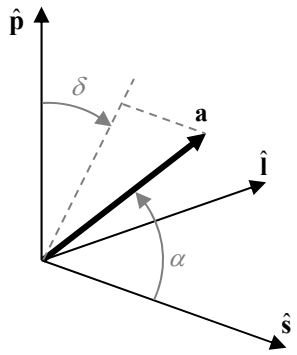

Figure 2 Definition of cone, α, and clock, δ, angles of the solar sail acceleration vector in $S\left(\hat{\mathbf{s}},\hat{\mathbf{l}},\hat{\mathbf{p}}\right)$ reference frame.

The blade's cone angle in Eq. (1) is defined in the $S\left(\hat{\mathbf{s}},\hat{\mathbf{l}},\hat{\mathbf{p}}\right)$ reference frame as illustrated in Figure 2. To compute the cone angle, first the Sun-direction is transformed from the Sun $S\left(\hat{\mathbf{s}},\hat{\mathbf{l}},\hat{\mathbf{p}}\right)$ reference frame, $\hat{\mathbf{s}}_S=\begin{bmatrix}1 & 0 & 0\end{bmatrix}^T$, into the i^{th} blade $L_i\left(\hat{\mathbf{l}}_1,\hat{\mathbf{l}}_2,\hat{\mathbf{l}}_3\right)$ reference frame using the transformation

$$\hat{\mathbf{s}}_S=\left[SD\right]\left[DB\right]\left[BL_i\right]\hat{\mathbf{s}}_{L_i} \tag{2}$$

with the rotation matrices $\left[SD\right]$, $\left[DB\right]$, and $\left[BL_i\right]$ defined in the Appendix. The blade's normal vector can be defined in the $L_i\left(\hat{\mathbf{l}}_1,\hat{\mathbf{l}}_2,\hat{\mathbf{l}}_3\right)$ frame as

$$\hat{\mathbf{n}}_{L_i} = \begin{bmatrix} 0 & 0 & \text{sign}\left(s_{L_i,3}\right) \end{bmatrix}^T \tag{3}$$

where $s_{L_i,3}$ is the third component of the $\hat{\mathbf{s}}_{L_i}$ unit vector, and the sign function ensures the sail normal points away from the Sun. The blade's cone angle can then be computed from

$$\cos\alpha_i = \hat{\mathbf{s}}_{L_i} \cdot \hat{\mathbf{n}}_{L_i} \,. \tag{4}$$

To obtain the *total* solar radiation pressure acceleration on all N blades of the heliogyro in the $S\left(\hat{\mathbf{s}},\hat{\mathbf{l}},\hat{\mathbf{p}}\right)$, $D\left(\hat{\mathbf{d}}_1,\hat{\mathbf{d}}_2,\hat{\mathbf{d}}_3\right)$ or $B\left(\hat{\mathbf{b}}_1,\hat{\mathbf{b}}_2,\hat{\mathbf{b}}_3\right)$ reference frames, the individual $\mathbf{a}_{i,L_i}$ acceleration components need to be transformed to the respective frame and summed. For the Sun $S\left(\hat{\mathbf{s}},\hat{\mathbf{l}},\hat{\mathbf{p}}\right)$ reference frame this becomes

$$\mathbf{a}_S = [SD][DB]\sum_{i=1}^{N}[BL_i]\mathbf{a}_{i,L_i} \,. \tag{5}$$

Because the heliogyro rotates, Eqs. (1) and (5) only provide the *instantaneous* acceleration vector. Equation (5) therefore needs to be averaged over one or two revolutions (depending on the selected blade pitch profile per Section III). This averaged acceleration vector, $\tilde{\mathbf{a}}_S$, can be obtained by integrating a single-blade heliogyro with respect to its azimuth angle, ψ_1, see Figure 1b [8]. This approach is valid because the integral is the same for each blade. The average acceleration for all blades can thus be obtained by evaluating the integral for one blade only, as long as this integral is multiplied by the total sail area A (not by the area of one blade A_i):

$$\tilde{\mathbf{a}}_S = 2P\frac{A}{m}\frac{1}{4\pi}[SD]\int_0^{4\pi}\left(\hat{\mathbf{s}}_{L_1}\cdot\hat{\mathbf{n}}_{L_1}\right)^2[DB][BL_1]\hat{\mathbf{n}}_{L_1}d\psi_1 \,. \tag{6}$$

Note that no analytical solution to Eq. (6) was found. It is therefore evaluated numerically.

The term $2PA_i/m$ in Eq. (1) is usually rewritten using the so-called characteristic acceleration, $a_{c,i}$. The characteristic acceleration is the solar radiation pressure acceleration that the sail or heliogyro blade can achieve when facing the Sun (i.e., $\alpha_i = 0$) at $r_{AU} = 1$ AU and at rest in the $S\left(\hat{\mathbf{s}},\hat{\mathbf{l}},\hat{\mathbf{p}}\right)$-frame:

$$a_{c,i} = \beta_i\frac{\mu_\odot}{r_{AU}^2}, \quad \beta = \sum_{i=1}^{N}\beta_i \tag{7}$$

with $\mu_\odot$ the gravitational parameter of the Sun and β the solar sail lightness number (ratio of solar radiation pressure acceleration to gravitational acceleration at the same location and time). Note that β_i refers to the lightness number of a single heliogyro blade and is computed using the blade's area and the total spacecraft mass. For N blades with the same size and material properties, each blade has a lightness number equal to $1/N$ of the lightness number of the entire spacecraft. At any other distance from the Sun, $r_\odot$, the acceleration of Eq. (1) becomes:

$$\mathbf{a}_{i,L_i} = \beta_i \frac{\mu_\odot}{r_\odot^2} \cos^2 \alpha_i \hat{\mathbf{n}}_{L_i} . \tag{8}$$

This paper assumes a baseline lightness number of the entire spacecraft of $\beta = 0.0363$ based on the expected performance of relatively mature FPF sail technology designed for the previously-proposed Sunjammer mission [11]. For an ideal solar sail reflectance model, this lightness number corresponds to a sail area of A_{sail} = 1068 m^2 for a 45 kg spacecraft mass [11]. Note that, due to the reduced sail system mass, a near-term value for a similarly-mature heliogyro-type sail would be approximately $\beta = 0.08$ [5].

III. Heliogyro pitch profiles

The blade pitch angle, θ_i (see Figure 1c), depends on the pitch profile selected and is required to compute the $[BL_i]$ transformation matrix. Reference [6] and many following works (e.g., References [5, 7, 8, 18]) define three different pitch profiles, which can be used independently or in combination:

1. Collective profile ('co')
2. ½-Period cyclic profile (half-p, 'hp')
3. 1-Period cyclic profile (cyclic, 'cy')

The 'co' profile pitches the blades constantly while the heliogyro rotates, while the 'hp'- and 'cy'-profiles pitch the blades sinusoidally with revolution. The 'hp' profile repeats after two revolutions (requiring the total acceleration vector in Eq. (6) to be averaged over two revolutions), while the 'cy' profile repeats after one revolution. Each of the pitch profiles and its effect on the solar radiation pressure force and moment is illustrated in Figure 3, which is taken from Reference [18]. Note that variants of these pitch profiles can be defined such as the attenuate profile, which is similar to the collective profile but pitches each blade in the opposite direction. The choice of which pitch profile to use will depend on the profile that can generate the desired solar radiation pressure

accelerations for orbital control without generating any adverse moments. Note that zero-moment about each body axis can be achieved with the attenuate profile for any pitch amplitude and attitude of the heliogyro.

Reference [8] provides the i^{th} blade's pitch angle for any combination of the three pitch profiles itemized above:

$$\theta_i = -a_{co} + a_{hp} \sin\left[\frac{1}{2}\left(\psi_i - \phi_{hp} - \text{sign}\left(a_{hp}\right)\frac{\pi}{2}\right)\right] + a_{cy} \sin\left(\psi_i - \phi_{cy}\right) \tag{9}$$

where a_{co}, a_{hp}, and a_{cy} are the amplitudes of the collective, half-p and cyclic profiles, respectively, and ϕ_{hp} and ϕ_{cy} are the phase angles of the half-p and cyclic profiles, respectively.

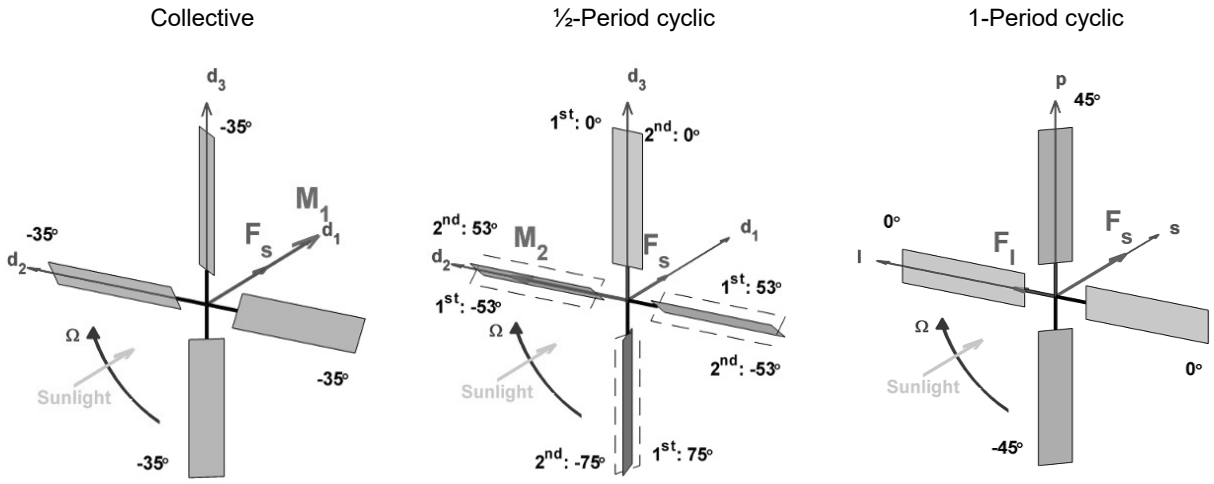

Figure 3 Illustration of pitch profiles for Sun-facing heliogyro ($\eta = 0$) (source: [18]).

IV. Heliogyro force capabilities

For an FPF (fixed-area) non-spinning solar sail at 1 AU, tilted with respect to the Sun direction at a cone angle α (where $\alpha = \eta$) and a clock angle $\delta = \frac{\pi}{2}$ (or $\gamma = 0$), see Figure 2, the normal vector to the sail area, $\hat{\mathbf{m}}$, can be written in the $S\left(\hat{\mathbf{s}}, \hat{\mathbf{l}}, \hat{\mathbf{p}}\right)$ reference frame as

$$\hat{\mathbf{m}}_S = \begin{bmatrix}\cos\alpha & \sin\alpha & 0\end{bmatrix}^T, \quad \alpha \in \left[-90^o, 90^o\right]. \tag{10}$$

The solar radiation pressure force that such an FPF (fixed-area) sail can achieve at 1 AU, per square meter sail area, and in the direction along the Sun line, F_s, and perpendicular to it, F_l, can be obtained from an equation

analogous to Eq. (1) or (8). Considering an interval for the cone angle of $\alpha \in \left[-90^o, 90^o\right]$, the result is the surface of a "bubble-shaped" force curve as shown in Figure 4a.

When transforming this force curve into an acceleration for a Sunjammer-type sail, the solid curve indicated with $\beta = 0.0363$ in Figure 4b is obtained. The other, dashed curves in Figure 4b are obtained when considering an FPF solar sail with four control vanes. Through the use of the vanes, the solar sail area can be scaled up and down by $2A_{vane}$, up to a maximum and minimum value of $A_{sail} + 2A_{vane}$ and $A_{sail} - 2A_{vane}$, respectively, with A_{vane} the sail area of a single vane. Note that, here, A_{sail} is the average solar sail area (not just referring to the main sail) and that the lightness number scales proportionally with these changes in sail area. Using a vane area of 15 m^2, as previously proposed for Sunjammer [20], the vanes enable an increase or decrease in the nominal sail area, and thus in the lightness number, of 2.8 percent: $\beta_{min} = 0.03528 \le \beta \le 0.03732 = \beta_{max}$. This FPF sail with vanes can thus achieve the thin volume shown in the shaded (a_s, a_l)-combinations in Figure 4b.

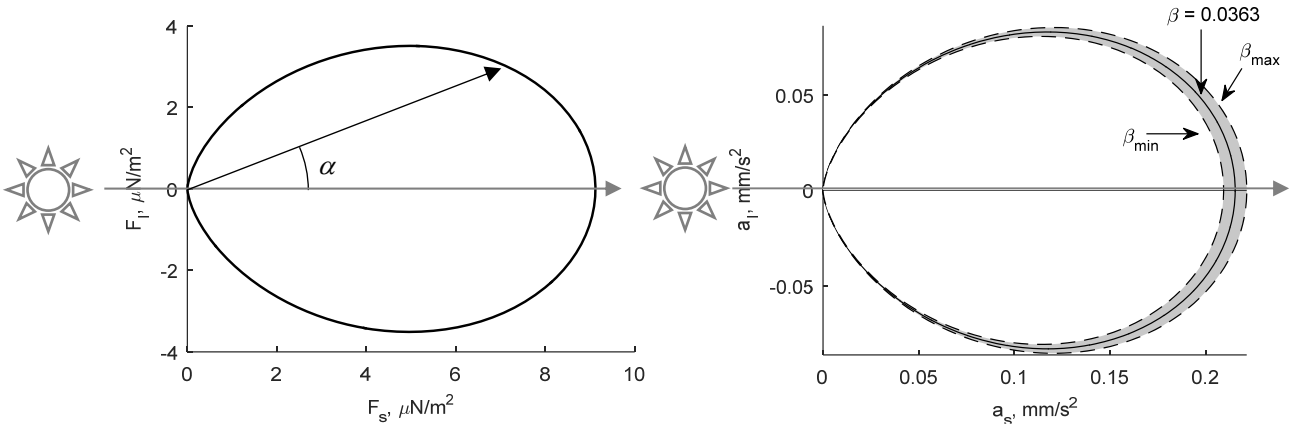

a) **b)**

Figure 4 FPF solar sail "bubble-shaped" force curve at 1 AU for α = [-90, 90] deg. a) Force per square meter sail area for a fixed area sail. b) Acceleration for fixed area sail and sail with control vanes.

When now considering a heliogyro, the ability to pitch its blades (in a collective, cyclic, or half-p manner as described in Figure 3) provides achievable *spin averaged* (F_s, F_l)- and (a_s, a_l)-combinations that are not constrained to the surface of the bubble for an FPF (fixed area) sail nor to the thin shaded volume for an FPF sail with vanes as in Figure 4b, but can instead take on any value within the whole bubble volume. This implies that the solar radiation pressure acceleration vector can be oriented away from the heliogyro's spin axis. This is

demonstrated in Figure 5, which shows averaged force contours of equal pitch amplitudes for the collective, half-p and cyclic pitch profiles. Each curve represents one specific amplitude of one of the profiles and is constructed by considering heliogyro attitudes of $\eta = \left[-90^o, 90^o\right]$ and assuming that the angle γ equals zero (see Figure 1a). Extending the results to non-zero values for γ gives the force curves of Figure 6. The figure shows that a non-zero γ angle rotates the two-dimensional "bubble-shaped" force curves around the $\hat{\mathbf{s}}$ -axis (Sun-spacecraft line).

The results in Figure 5 and Figure 6 show that a heliogyro can be modelled as an FPF sail with a highly-variable lightness number, allowing it to scale the solar radiation pressure force between zero and that of an equivalent-area FPF solar sail. Note that for the cases considered in Figure 5 (i.e., $\phi_{hp} = 0$ and $\phi_{cy} = 0$) the half-p and cyclic profiles cannot generate *all* combinations of the force magnitude and direction in the interior of the bubble, as shown by the black infeasible regions in the plots on the right hand side of Figure 5b and c. However, these regions can be captured by using a collective profile, which *does* allow any combination of the force magnitude and direction in the interior to be reached. It is this property of a heliogyro, i.e., enabling a highly-variable lightness number (more variable than that of an FPF sail with vanes), which is exploited in this paper for orbital control. In particular, it is used here to correct for injection errors and solar sail deployment failure at injection into a solar sail Sun-Earth sub-L_1 solar sail halo orbit.

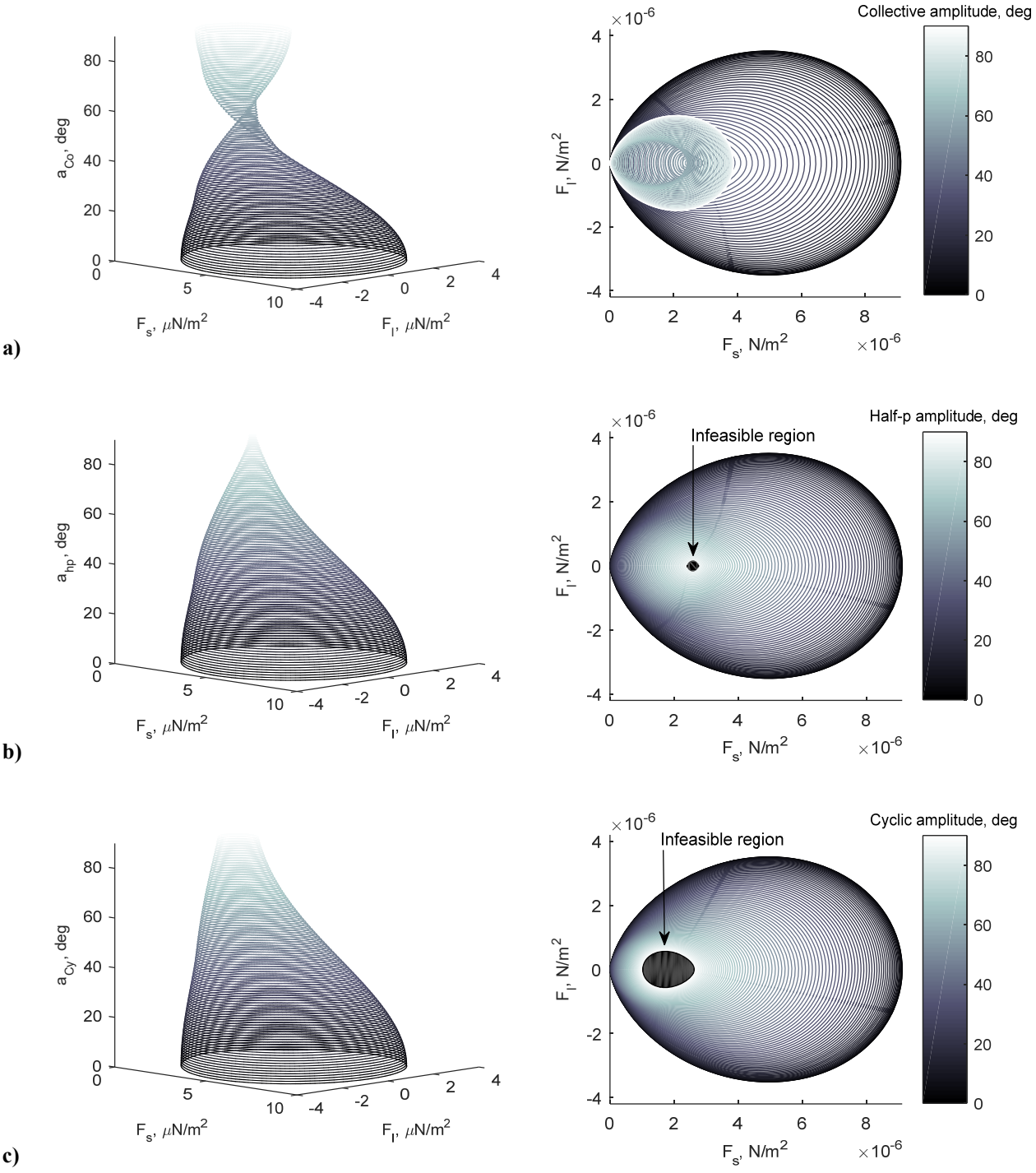

Figure 5 Heliogyro "bubble-shaped" force curves providing the average force per square meter sail area at 1 AU for η = [-90, 90] deg, γ = 0 deg, and different heliogyro blade pitch profiles and profile amplitudes. a) Collective profile. b) Half-p profile, ϕ_{hp} = 0. c) Cyclic profile, ϕ_{cy} = 0.

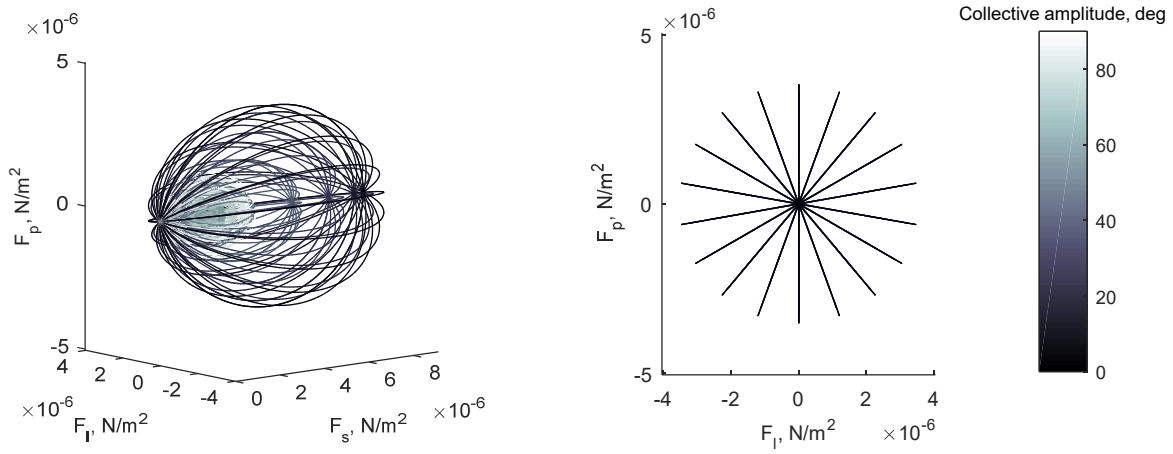

Figure 6 Heliogyro "bubble-shaped" force curves for a collective profile, providing the average force per square meter sail area at 1 AU for η = [-90, 90] deg and γ = [-90,90].

V. Solar sail Sun-Earth L_1 halo orbits

One near-term application of solar sail technology is an advanced space weather forecasting platform at a sub-L_1 location [12]. In reality, the sail cannot be placed exactly *on* the Sun-Earth line as this causes solar radio interference during communications. The sail would have to reside in a solar sail halo orbit around the sub-L_1 point such that it orbits a 5 deg solar exclusion zone (SEZ) [21]. The generation of solar sail halo orbits has been investigated before (e.g., References [22-24]), and the approach is briefly repeated here, starting with the solar sail dynamics in the Sun-Earth circular restricted three-body problem (CR3BP). Note that the eccentricity of the Earth's orbit makes a significant difference in the details of such orbits [13], but the CR3BP is used here to investigate the fundamental advantages of the heliogyro over an FPF sail in this application.

A. Solar sail Sun-Earth circular restricted three-body problem

As a summary of more extensive works on the CR3BP (e.g., Reference [25]), the CR3BP can be characterized as a framework that describes the motion of an infinitesimal mass, m (here the sailcraft), under the influence of the gravitational attraction of two much larger primary masses, m_1 (the Sun) and m_2 (the Earth). The CR3BP further assumes that the gravitational influence of the sailcraft on the Sun and Earth can be neglected and that the Sun and Earth move in circular orbits about their common barycenter O. Figure 7 shows the synodic reference frame employed in the CR3BP, $C(\hat{\mathbf{x}}, \hat{\mathbf{y}}, \hat{\mathbf{z}})$, that rotates such that the Sun and Earth remain on the x-axis. A set of

canonical units is used where the Sun-Earth system mass, the Sun-Earth distance and the frame's angular velocity, $\boldsymbol{\omega}_C = \omega\hat{\mathbf{z}}$, are set to unity and the mass ratio $\mu = m_2/(m_1+m_2) = 3.0404\times10^{-6}$ is defined. Note that the subscript C refers to the synodic reference frame.

In the synodic reference system, the motion of the solar sail is described by [1]

$$\ddot{\mathbf{r}}_C + 2\boldsymbol{\omega}_C \times \dot{\mathbf{r}}_C = \mathbf{a}_C - \nabla U \tag{11}$$

with $\mathbf{r}_C = \begin{bmatrix} x & y & z \end{bmatrix}^T$ the position vector of the sail, $U = -\frac{1}{2}\left(x^2+y^2\right) - \left(\left[1-\mu\right]/r_{C,1} + \mu/r_{C,2}\right)$ the effective potential that combines the gravitational potential and the potential from the centripetal acceleration, and $\mathbf{a}_C$ the solar sail acceleration expressed in the CR3BP reference frame, which for an FPF solar sail equals:

$$\mathbf{a}_C = \beta\frac{1-\mu}{r_{C,1}^2}\left(\hat{\mathbf{m}}_C \cdot \hat{\mathbf{r}}_{C,1}\right)^2 \hat{\mathbf{m}}_C \tag{12}$$

with the vectors $\mathbf{r}_{C,1}$ and $\mathbf{r}_{C,2}$ defined as $\mathbf{r}_{C,1} = \begin{bmatrix} x+\mu & y & z \end{bmatrix}^T$ and $\mathbf{r}_{C,2} = \begin{bmatrix} x-(1-\mu) & y & z \end{bmatrix}^T$.

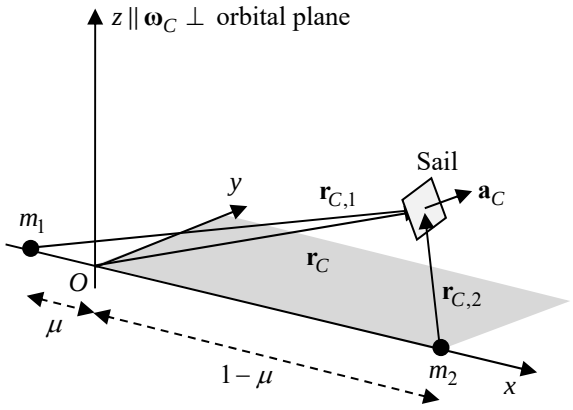

Figure 7 Schematic of solar sail circular restricted three-body problem.

B. Solar sail halo orbits

Many works in the literature (e.g., References [22-24, 26-28]) describe methods to find solar sail periodic (halo) orbits under the dynamics described in Eq. (11) or similar systems. In this paper, the approach of Reference [24] is

adopted, which shows that solar sail halo orbits exist under different sail steering laws, e.g., $\hat{\mathbf{m}}_C = \hat{\mathbf{r}}_{C,1}$ (Sun-pointing) or $\hat{\mathbf{m}}_C = \begin{bmatrix} 1 & 0 & 0 \end{bmatrix}^T$ (synodic x-pointing). In this work, the latter steering law is adopted.

The process for finding a halo orbit is initialized by approximating the equations of motion in Eq. (11) in the neighborhood of the sub-L_1 point by linearization, but expanding the effective potential and solar sail acceleration terms to third order with a Taylor series. The Lindstedt-Poincaré method is subsequently used to find the third order solution to this approximated dynamical system. Details on the method can be found in Reference [24]. As these solutions only hold in the linearized system, the orbit quickly diverges when it is integrated in the full non-linear system of Eq. (11). A differential correction scheme is therefore applied to correct the initial conditions of the approximated orbit to find closed solar sail halo orbits in the full non-linear system. This is used to find solar sail halo orbits with small amplitudes, i.e., close to the sub-L_1 point. A continuation scheme is subsequently applied to gradually increase the orbit's out-of-plane amplitude until the orbit remains outside the 5 deg SEZ.

The resulting solar sail halo orbit for a Sunjammer-type sail, i.e., $\beta = 0.0363$ is presented in Figure 8a, with initial conditions as

$$\mathbf{x}_{C,0} = \begin{bmatrix} \mathbf{r}_{C,0} & \dot{\mathbf{r}}_{C,0} \end{bmatrix}^T = \begin{bmatrix} 0.9798 & 0 & 0.0018 & 0 & 0.0128 & 0 \end{bmatrix}^T . \tag{13}$$

This initial condition corresponds to the most northern (i.e., out-of-ecliptic) location of a solar sail halo orbit with average in- and out-of-plane amplitudes of approximately 1.25×10^6 and 2.5×10^5 km, respectively. The additional dots in Figure 8a indicate the initial conditions of other orbits in the family of solar sail halo orbits for $\beta = 0.0363$ and $\hat{\mathbf{m}}_C = \begin{bmatrix} 1 & 0 & 0 \end{bmatrix}^T$, clearly indicating how the family evolves from lying within the SEZ to orbits orbiting around the SEZ. For reference, these orbits have periods of approximately 268 days. Solar sail halo orbits for other values for the lightness number are provided in Figure 8b which is a side-view to clearly show how the orbit is displaced further Sunward for increasing values of β. At the point closest to the Sun and compared to a satellite at the L_1 point, these orbits increase the solar storm warning time by a factor 1.3 to 4.4.

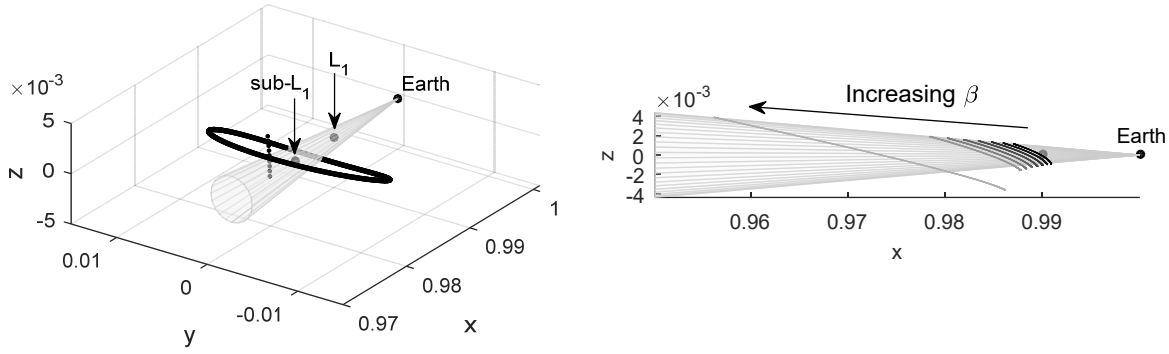

a) **b)**

Figure 8 Solar sail halo orbits fitting around a 5 deg solar exclusion zone. a) $\beta = 0.0363$ with dots indicating initial conditions of family of solar sail halo orbits for $\beta = 0.0363$. b) (*x*,*z*)-view for $\beta = 0.01$ - 0.04 and 0.08.

VI. Linear-quadratic controller

To investigate the orbital control capabilities of a heliogyro, this paper investigates how well the heliogyro can recover from errors on the orbit injection and from solar sail deployment delays at injection. To this end, an LQR feedback control approach is used to generate reasonable sailcraft control actions in response to these initial condition errors, similar to the works in References [13, 14, 29-31]. The MATLAB/Simulink® diagram of the LQR algorithm is provided in Figure 9.

As a result of the injection error or delayed solar sail deployment, the trajectory, $\mathbf{x}$, will deviate from the nominal solar sail halo orbit, i.e., the nominal trajectory, $\mathbf{x}_{nom}$. The error on the state, $\delta\mathbf{x} = \mathbf{x} - \mathbf{x}_{nom}$ is used to compute the required feedback control, $\delta\mathbf{u}$, which is added to the nominal control to obtain the total control, $\mathbf{u} = \mathbf{u}_{nom} + \delta\mathbf{u}$. Given sufficient control authority, this total control should bring the trajectory back to the nominal trajectory after some time. If the state error is small, i.e., the sailcraft remains close to the reference trajectory, the system dynamics can be described by linearizing the equations of motion in Eq. (11) around the nominal conditions. For that, Eq. (11) is rewritten as a set of first order differential equations:

$$\dot{\mathbf{x}}(t) = \mathbf{f}\left(\mathbf{x}(t), \mathbf{u}(t), t\right) \tag{14}$$

to obtain

$$\delta\dot{\mathbf{x}} = \mathbf{A}\delta\mathbf{x} + \mathbf{B}\delta\mathbf{u} \tag{15}$$

with

$$\mathbf{A}_{6x6} = \left[\frac{\partial \mathbf{f}}{\partial \mathbf{x}}\right]_{\mathbf{x}_{nom},\mathbf{u}_{nom}}, \quad \mathbf{B}_{6x3} = \left[\frac{\partial \mathbf{f}}{\partial \mathbf{u}}\right]_{\mathbf{x}_{nom},\mathbf{u}_{nom}}. \tag{16}$$

Note that the linearization about points on the nominal halo orbit results in a time varying linear system in Eq. (15), but the notation of the time dependency is omitted for brevity. An infinite-horizon quadratic cost function is used

$$J = \int_0^\infty \left(\delta\mathbf{x}^T\mathbf{Q}\delta\mathbf{x} + \delta\mathbf{u}^T\mathbf{R}\delta\mathbf{u}\right)dt, \tag{17}$$

where the first and second terms on the right hand side of Eq. (17) penalize the transient state error and control effort, respectively. The weighing matrices $\mathbf{Q}_{6x6} = 10,000\mathbf{I}_{6x6}$ and $\mathbf{R}_{3x3} = \mathbf{I}_{3x3}$ were chosen to result in reasonable control effort and control performance in this application. Note that the same scaling factor is applied to the position- and velocity-related components of the matrix $\mathbf{Q}$, because in the canonical units of the CR3BP the position and velocity are of equal order of magnitude. In addition, the position and velocity need to be tracked equally well in order to remain in the neighbourhood of the halo orbit and maintain the halo orbit over time.

The control that minimizes the value of the cost J (assuming time-invariant $\mathbf{A}$ and $\mathbf{B}$) is the feedback law

$$\delta\mathbf{u} = -\mathbf{K}\delta\mathbf{x} \tag{18}$$

with the constant gain matrix $\mathbf{K}_{3x6}$ found using the Matlab® function *lqr(A,B,Q,R)*. This solution is re-computed at each integration step, resulting in a time-varying gain matrix $\mathbf{K}$. For the solar sail halo orbit of Figure 8a, most elements of the gain matrix oscillate around a value close to zero. The difference between the minimum and maximum value therefore never exceeds a factor 2.4 (where a factor of two reflects oscillation around zero) and the maximum rate of change in any element of the gain matrix is in the order of 10^{-4} s^{-1}.

For comparison, the solar sail halo orbits will be controlled both with an FPF sail with vanes (hereafter referred to in short as FPF sail) and a heliogyro, where (according to the findings in Section IV) the heliogyro is modelled as an FPF sail with a highly varying lightness number. For both configurations, the control components then include the direction of the sail's acceleration vector, which is described using the cone and clock angles, α and δ (see

Figure 2). In addition, to account for the effect of the variable area effect of control vanes and of pitching the heliogyro's blades, the lightness number is added as a control, resulting in $\mathbf{u}(t)=\left[\alpha(t) \quad \delta(t) \quad \beta(t)\right]^T$. Note that the nominal control consists of the cone and clock angles required to achieve $\hat{\mathbf{m}}_C=\left[1 \quad 0 \quad 0\right]^T$ (synodic x-pointing) along the solar sail halo orbit and a corresponding constant value for the lightness number, β_{nom}. The block diagram in Figure 9 shows that bounds are enforced on these control components

$$\begin{aligned} -90^o \le \alpha \le 90^o \\ -\infty \le \delta \le \infty \\ \beta_{min} \le \beta \le \beta_{max} \end{aligned} \tag{19}$$

where the bounds on the lightness number are defined as:

$$\begin{aligned} \beta_{min} &= \begin{cases} (1-0.028)\beta_{nom} & \text{FPF sail} \\ 0 & \text{Heliogyro} \end{cases} \\ \beta_{max} &= \begin{cases} (1+0.028)\beta_{nom} & \text{FPF sail} \\ \beta_{max} & \text{Heliogyro} \end{cases} \end{aligned} \tag{20}$$

For the heliogyro, different values for the upper bound of the lightness number, β_{max}, are assumed, including the upper bound for the FPF sail configuration.

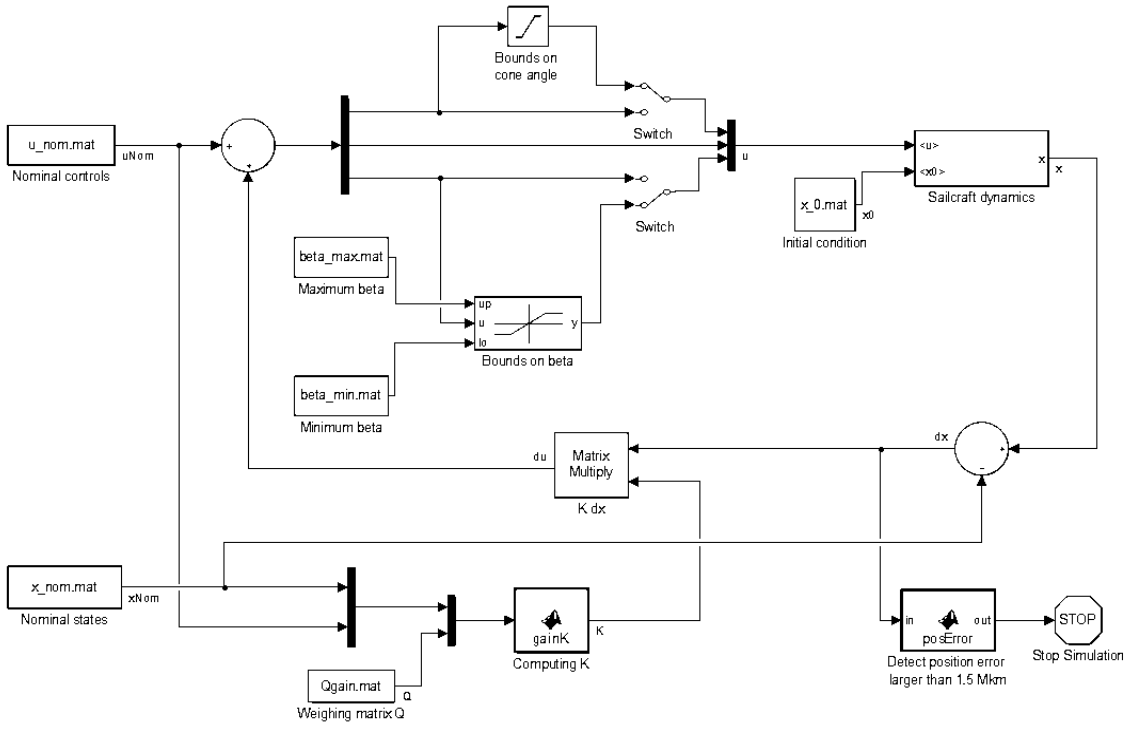

Figure 9 Matlab/Simulink® diagram of LQR for solar sail halo orbit control.

A. Injection error

The first test case of this paper considers injection errors into the solar sail halo orbit. This injection error is modelled by perturbing the initial condition of the solar sail, see Eq. (13), as

$$\mathbf{x}_{C,0} = \begin{bmatrix} \mathbf{r}_{C,0} + \Delta\mathbf{r}_0 \\ \dot{\mathbf{r}}_{C,0} + \Delta\dot{\mathbf{r}}_0 \end{bmatrix}, \tag{21}$$

where the perturbation is provided in the direction of the unstable eigenvector, $\boldsymbol{\xi}$, corresponding to the eigenvalue with $|\lambda_j| > 1$ of the one-orbit discrete state transition matrix of the nominal orbit. This test case is intended to explore the worst case orbit injection errors, as these should tend to require the largest control effort. With $\boldsymbol{\xi} = \begin{bmatrix} \boldsymbol{\xi}_{pos} & \boldsymbol{\xi}_{vel} \end{bmatrix}^T$, the perturbations become $\Delta\mathbf{r}_0 = \Delta r_0 \boldsymbol{\xi}_{pos}$ and $\Delta\dot{\mathbf{r}}_0 = \Delta\dot{r}_0 \boldsymbol{\xi}_{vel}$. The position error component of this perturbation is illustrated in Figure 10a, where the gray arrow indicates the unstable eigenvector direction and the round marker the location along this direction where injection actually takes place. Section 7 will present results for a large range of perturbation magnitudes, Δr_0 and $\Delta\dot{r}_0$, both positive and negative, where negative values for the perturbation represent an injection error in the $-\boldsymbol{\xi}$-direction (i.e., Earthward of the nominal injection location). Note that, only for $\Delta r_0 = \Delta\dot{r}_0$ is the eigendirection perturbation preserved, but that additional perturbation magnitudes are considered (i.e. $\Delta r_0 \neq \Delta\dot{r}_0$) to expand the design space to include additional, realistic injection error cases.

B. Time delay in solar sail deployment

The second test case of this paper considers a solar sail deployment failure upon injection into the solar sail halo orbit. Here the orbit injection is assumed to be accurate, resulting in a position and velocity on the desired halo, but because the sail does not deploy on time, the sailcraft will drift away from the halo orbit according to the classical (no solar radiation pressure) CR3BP dynamics. This is illustrated by the black dashed trajectory in Figure 10b. Once the sail deploys, the position and velocity at that point are used as initial condition perturbations for the LQR control evaluation. Note that the position error in this case is similar to that of the orbit injection error case (for $\Delta r_0 > 0$), but the resulting velocities are in quite different directions.

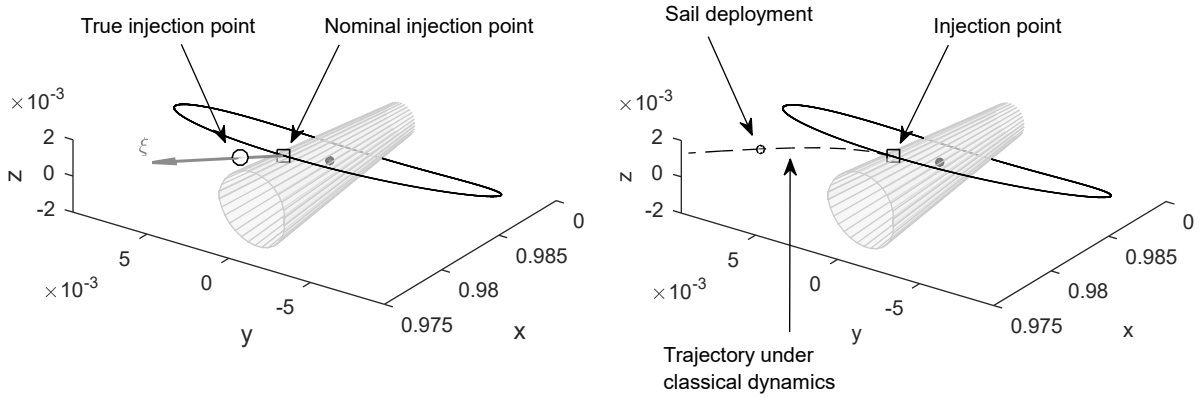

Figure 10 Illustration of test cases for β_{nom} = 0.0363. a) 500,000 km error on the nominal injection position in direction of unstable eigenvector. b) Solar sail deployment delay with actual deployment after Δt_0 = 25 days.

C. LQR performance quantification

The control is considered successful if, after four nominal halo orbit periods (i.e., 2.9 years), the error on the position and velocity components are smaller than a tolerance, ε. An example for one position and one velocity coordinate is provided in Figure 11, where two dimensionless values for the tolerance are considered: a strict tolerance of $\varepsilon = 10^{-4}$, which corresponds to an allowable error on the position of 15,000 km and an allowable error on the velocity of 3 m/s, and a looser tolerance of $\varepsilon = 5\times10^{-4}$, corresponding to allowable errors of 75,000 km and 15 m/s. While the velocity coordinate in this example satisfies the stricter tolerance of $\varepsilon = 10^{-4}$, the velocity coordinate does not (within the time period shown), but it does satisfy the tolerance of $\varepsilon = 5\times10^{-4}$. As this example is representative of controlled behavior in this application, the LQR control is considered successful if the tolerance of $\varepsilon = 5\times10^{-4}$ is met. While the example in Figure 11 only considers two states, the error tolerance will be applied to each of the six solar sail states and all need to satisfy the error tolerance after four halo orbits in order for the control to be considered successful.

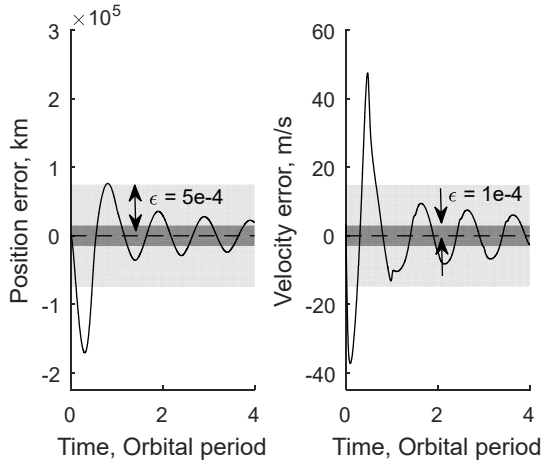

Figure 11 Example of state error to support definition of LQR performance quantification.

VII. Results

This section provides the results of the LQR feedback controller of Section VI to correct for injection errors and solar sail deployment failure at injection into the solar sail halo orbits of Section V.

A. Injection error

The first results, in Figure 12, are for a nominal lightness number equal to that of Sunjammer, i.e., $\beta_{nom} = 0.0363$. See Figure 8a for the corresponding solar sail halo orbit. Figure 12a and b provide, respectively, the recoverable injection error for an FPF solar sail and a heliogyro with the same upper limit on the lightness number of $\beta_{max} = (1+0.028)\beta_{nom} = 0.03732$ and for $\varepsilon = 5\times10^{-4}$. The only difference between the two sail configurations is thus the value for β_{min}. It is clear from Figure 12a and b (which are plotted on the same scale) that the heliogyro can correct for significantly larger injection errors in position and velocity than an FPF sail, at least for negative (Earthward) position errors. The FPF sail can only recover from injection errors that are approximately of the same magnitude as the controlled error tolerance ε (see the rectangular boxes in Figure 12). These initial results clearly show the effect of the heliogyro's capability of fully scaling down the lightness number. From an operational point of view, the results furthermore show that it is best to undershoot, i.e., intentionally inject slightly Earthward. This will artificially shift the nominal injection point to the center of the recoverable injection error surface of Figure 12b, from where greater errors both in Sunward and Earthward directions can be recovered.

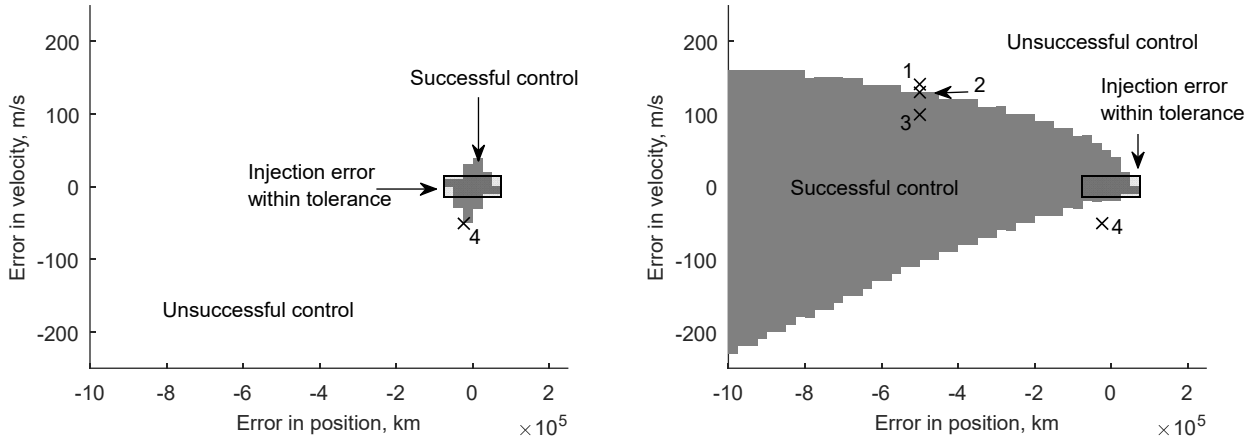

a) b)

Figure 12 Recoverable injection error for solar sail halo orbit with $\beta_{nom} = 0.0363$. Details for the cases numbered one through four are in Figure 13 and Figure 16. a) FPF sail. b) Heliogyro with $\beta_{max} = 0.03732$.

Details for the cases numbered one to three in Figure 12b are provided in Figure 13. These plots provide insight into the orbital control on the boundary of the recoverable injection error surface in Figure 12b. The plots on the left hand side of Figure 13 provide the state error over time. Note that these are plotted for an integration time of *eight* nominal halo orbit periods with the prescribed convergence time of four halo periods indicated with a black dotted line. The allowable error tolerance of $\varepsilon = 5\times10^{-4}$ is represented with a light gray band around the time axis, while a tighter tolerance of $\varepsilon = 10^{-4}$ is shown in dark gray (similar to Figure 11).

The right hand side of Figure 13 provides the direction of the solar sail acceleration (i.e., the cone and clock angles α and δ, see Figure 2) over time and the lightness number profiles, indicating the maximum lightness number of $\beta_{max} = 0.03732$ as well as the FPF sail's minimum lightness number of $\beta_{min} = 0.03528$ with dashed lines. From these three controls (α, δ, and β), the required solar radiation pressure acceleration vector can be computed. By subsequently defining an inverse problem and choosing a particular heliogyro blade pitch profile to provide this acceleration, the required pitch amplitude (and phase) and attitude of the heliogyro (in terms of the angles η and γ, see Figure 1a) can be obtained. Solving this inverse problem is highly complex (see for example References [8, 18] for the inverse problem for the heliogyro's solar radiation pressure moments) and is beyond the scope of the current investigation that is meant to demonstrate the fundamental advantages of the heliogyro over an FPF sail for the orbital control of solar sail halo orbits.

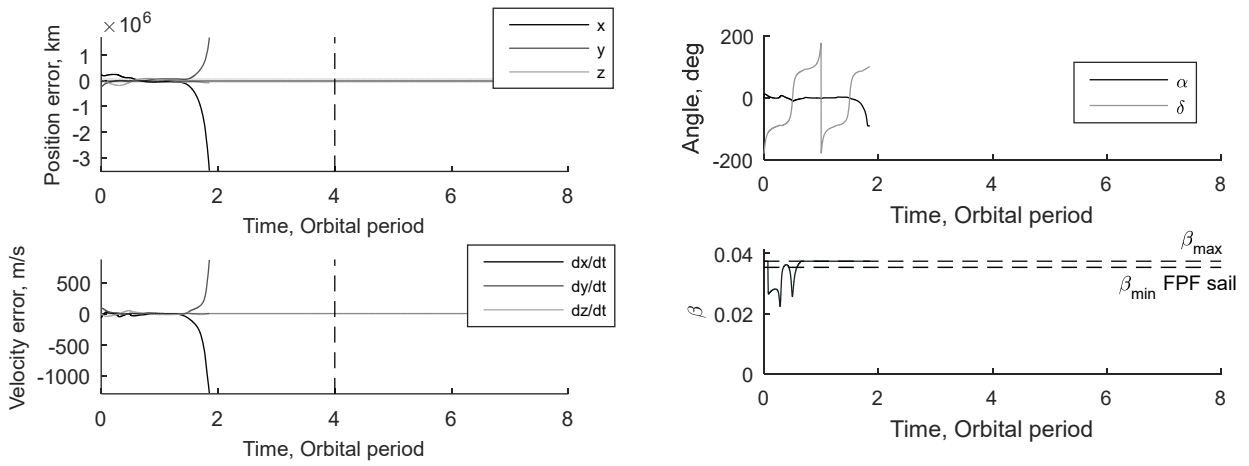

a)

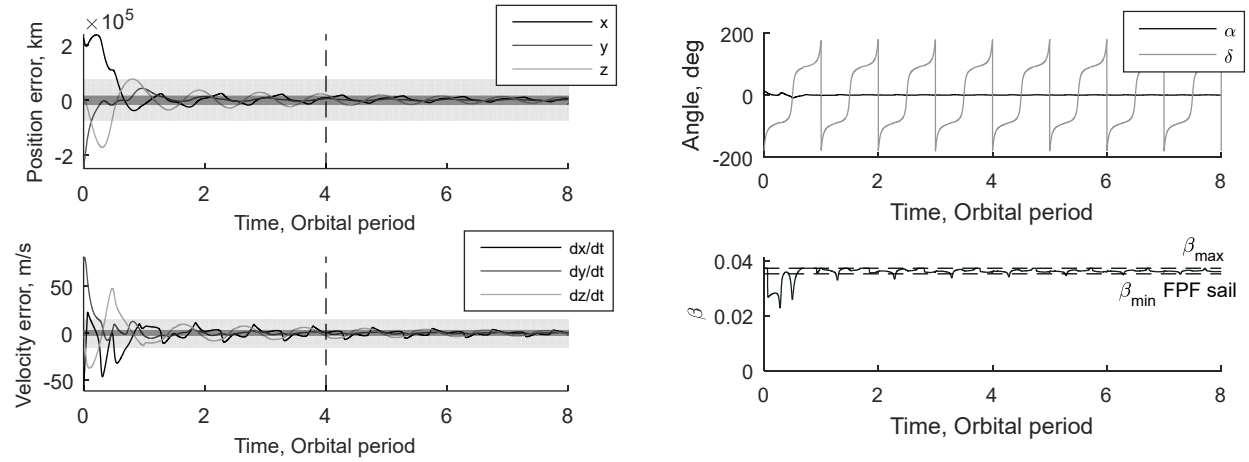

b)

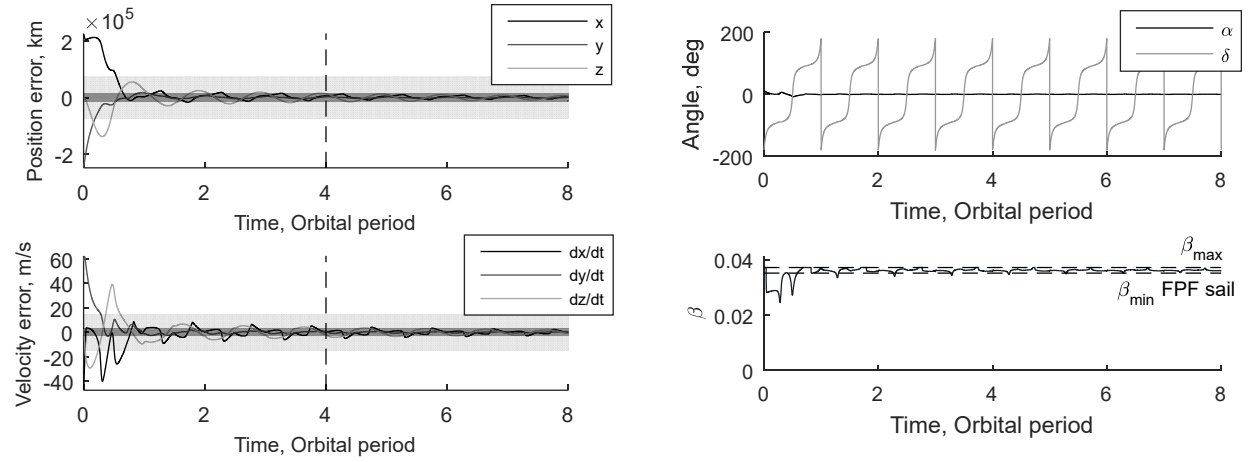

c)

Figure 13 Details for cases numbered one to three in Figure 12b. a) Case 1: Δr_0 = -500,000 km; $\Delta \dot{r}_0$ = 140 m/s. b) Case 2: Δr_0 = -500,000 km; $\Delta \dot{r}_0$ = 130 m/s. c) Case 3: Δr_0 = -500,000 km; $\Delta \dot{r}_0$ = 100 m/s.

For case 1 (Figure 13a), with Δr_0 = -500,000 km and $\Delta \dot{r}_0$ = 140 m/s, it is clear that the trajectory quickly diverges from the halo orbit and cannot be recovered even though the maximum lightness number is applied continuously towards the end of the control. (Note that for computational speed, propagation is truncated when the error on the position becomes larger than 1,500,000 km, which is considered an unrecoverable error).

For a slightly smaller error on the velocity (case 2: Figure 13 b), with Δr_0 = -500,000 km and $\Delta \dot{r}_0$ = 130 m/s, a completely different state error profile emerges where the error tolerance of $\varepsilon = 5 \times 10^{-4}$ is met within one nominal halo orbit period. The tighter tolerance of $\varepsilon = 10^{-4}$ is not met after four orbital periods, but the left plot in Figure 13b shows that by increasing the integration time, this tolerance can eventually be met. To show the effect of the error tolerance, Figure 14 is included, which shows how the surface of recoverable injection error changes when decreasing the error tolerance for the prescribed convergence time of four halo orbit periods. Note that further *in*creasing the tolerance does not give any gain in recoverable position or velocity errors: on the edge of the surface for $\varepsilon = 5 \times 10^{-4}$ a bifurcation takes place between dynamics with diverging trajectories (as in Figure 13a) and with recoverable errors (as in Figure 13b). The only way to move this bifurcation to larger errors in position and velocity is by increasing the value for β_{max} as will become clear later on in this section. Finally also note that the gap in the error surface for $\varepsilon = 10^{-4}$ and for large negative values for the error on position and velocity can be filled by once again increasing the prescribed convergence time (not shown), indicating that the error is still decreasing with time in this area.

Figure 15 provides the trajectory that brings the heliogyro back to the nominal halo orbit for case 2, where the detail also includes other neighboring nominal halo orbits for β_{nom} = 0.0363 (corresponding to the dots in Figure 8b). The figure clearly shows that the majority of the orbit is recovered in the first orbital revolution, bringing the sail back to the vicinity of the targeted halo orbit and seemingly onto an alternative solar sail halo orbit, oscillating around the target orbit as it slowly converges onto the target orbit. The control angle profiles in the right plot of Figure 13b show that this control can be achieved with very small cone angles, α, for the solar sail acceleration. The solar sail acceleration vector is thus almost aligned with the Sun-sail direction and oscillates around this Sun-sail direction once per halo orbit period (see the clock angle profile, δ).

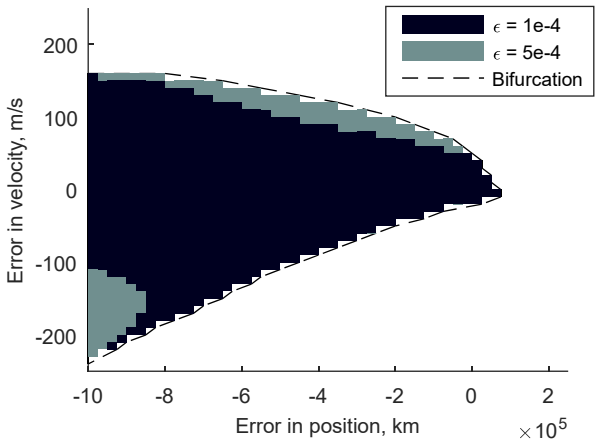

Figure 14 Heliogyro recoverable injection error for solar sail halo orbit with β_{nom} = 0.0363 and β_{max} = 0.03732 for different error tolerances.

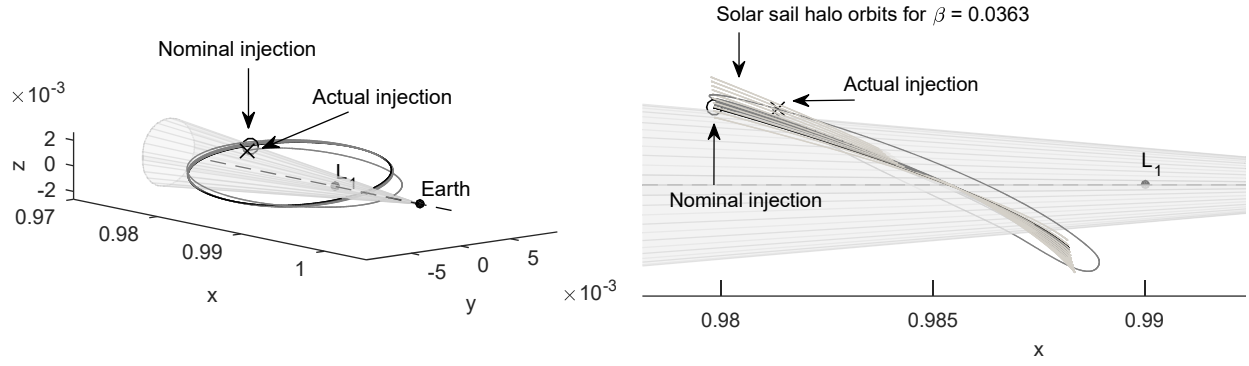

Figure 15 Trajectory for case 2 in Figure 12b: Δr_0 = -500,000 km; $\Delta \dot{r}_0$ = 130 m/s.

When decreasing the error on the velocity even further (case 3, Figure 13c with Δr_0 = -500,000 km; $\Delta \dot{r}_0$ = 100 m/s) both tolerances can be met with the heliogyro within the prescribed convergence time of four halo periods. For both successful controls (cases 2 and 3) the lightness number profiles show how the heliogyro eventually settles with the lightness number around the nominal value of 0.0363, as one would expect. Finally, the lightness number profiles also show that the LQR feedback controller requests lightness number values far below the minimum value for the FPF sail, showing that it is the unique capability of the heliogyro of being able to significantly reduce the lightness number that leads to successful control in these cases.

The final case to highlight is the one indicated as number four in Figure 12, with Δr_0 = -25,000 km and $\Delta \dot{r}_0$ = -50 m/s. This is one of very few cases where the FPF sail enables successful control, while the heliogyro does not. More details on this case are provided in Figure 16. The state error profiles in Figure 16a show that the trajectory quickly diverges from the halo orbit when controlled with a heliogyro, while successful control is achieved with the FPF sail configuration. The difference in performance can be explained by the difference in the lightness number profiles at the start of the control. From Figure 16b (right plot) it is clear that this particular case initially requests the minimum lightness number value, which, according to Eq. (20), equals $\beta_{min} = 0$ for the heliogyro and $\beta_{min} = 0.03528$ for an FPF sail. By "switching off" the sail in the case of the heliogyro, the sailcraft builds up an amount of momentum that cannot be countered by a subsequent increase in the lightness number up to a value of β_{max}. More symmetric control limits as imposed for the FPF sail would therefore be of benefit. This option will be explored next, by increasing the value for β_{max}.

The above has shown the influence of the lower bound on the lightness number on the control capabilities of the FPF sail and heliogyro configurations. It would therefore be of interest to investigate what the influence of the heliogyro's upper bound on the lightness number could be. Note that, increasing the value for β_{max} for the heliogyro configuration is justified because the heliogyro concept allows smaller sail loadings, enabling near-term lightness numbers of approximately $\beta = 0.08$, twice that of near-term FPF sail technology for the previously proposed Sunjammer mission. This larger lightness number can be used to place the sailcraft closer to the Sun for a further increase in the solar storm warning time, better control authority (as proposed in this paper), or a combination of these two objectives.

To show the effect of other values for β_{max} on the recoverable injection error, Figure 17 keeps all simulation parameters the same as those used to generate the results in Figure 12, only increasing the heliogyro's value for β_{max}. As can be expected, the larger the value for β_{max}, the larger the injection error that can be corrected for. Further details for case 1 of Figure 12 (Δr_0 = -500,000 km and $\Delta \dot{r}_0$ = 140 m/s), which did not lead to successful control for $\beta_{max} = 0.03732$, are provided in Figure 18 for additional β_{max}-values. Again, while a value of $\beta_{max} = 0.03732$ could not recover from these injection errors (see Figure 13a), values of $\beta_{max} \geq 0.038$ *can.* Figure

18 shows that the lightness number control profile is very similar for each value for $\beta_{max} \geq 0.038$ and only differ in the length of time that the maximum lightness number value is requested.

Finally, a similar conclusion can be drawn for case 4 of Figure 12, which also did not lead to successful control for the heliogyro, but was successful for the FPF sail configuration. When increasing the maximum lightness number value to $\beta_{max} \geq 0.04$, the errors in position and velocity of case 4 can be accommodated with a heliogyro.

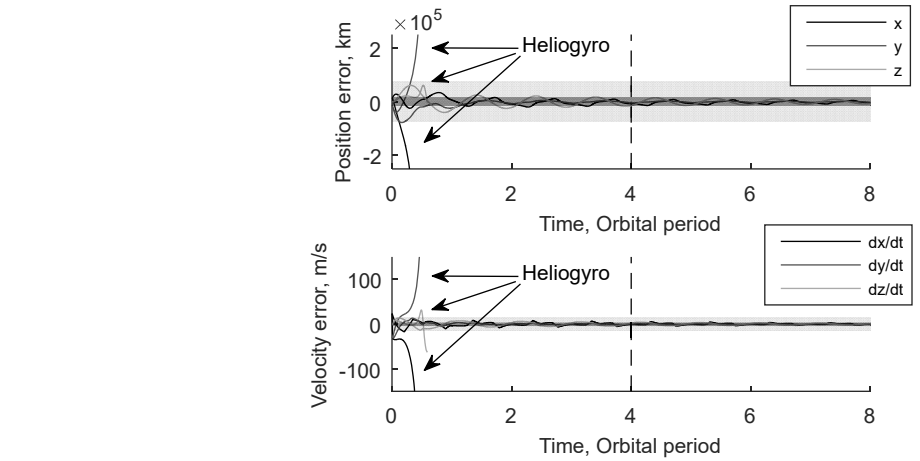

a)

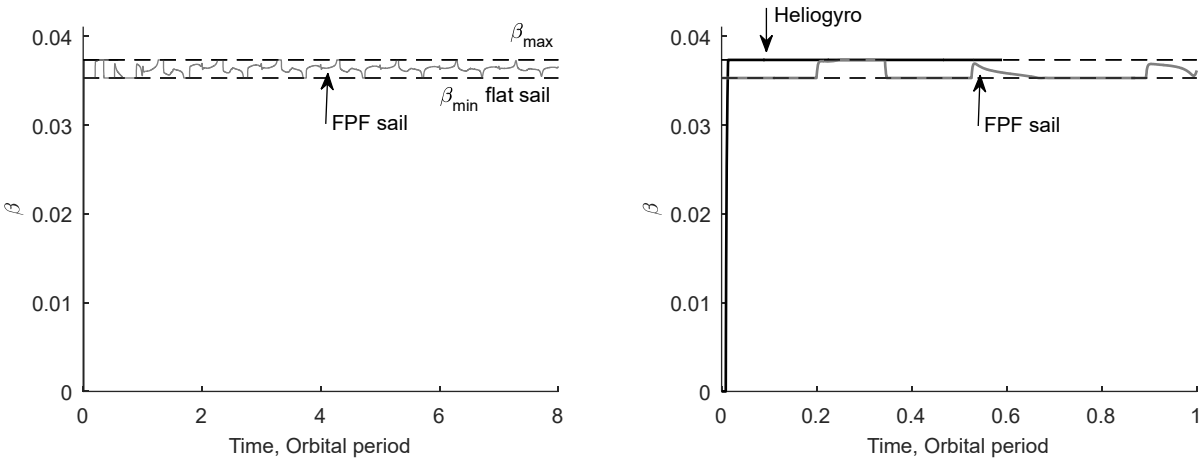

b)

Figure 16 Details for case 4 in Figure 12 for both FPF sail and heliogyro configurations. a) State errors. b) Lightness number profiles (the right plot is a detail of the left plot).

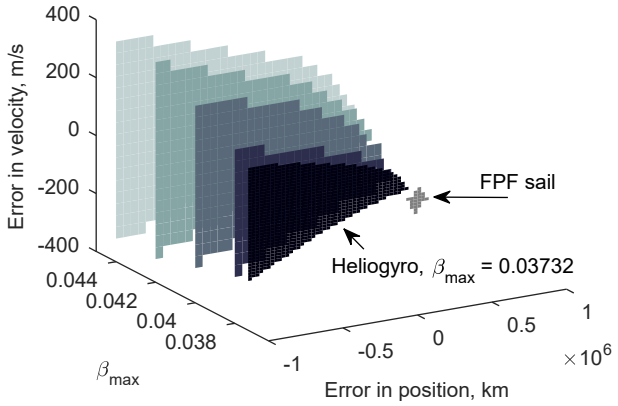

Figure 17 Orbital control of solar sail halo orbit with β_{nom}= 0.0363. Recoverable injection error for FPF sail and heliogyro with different values for β_{max}.

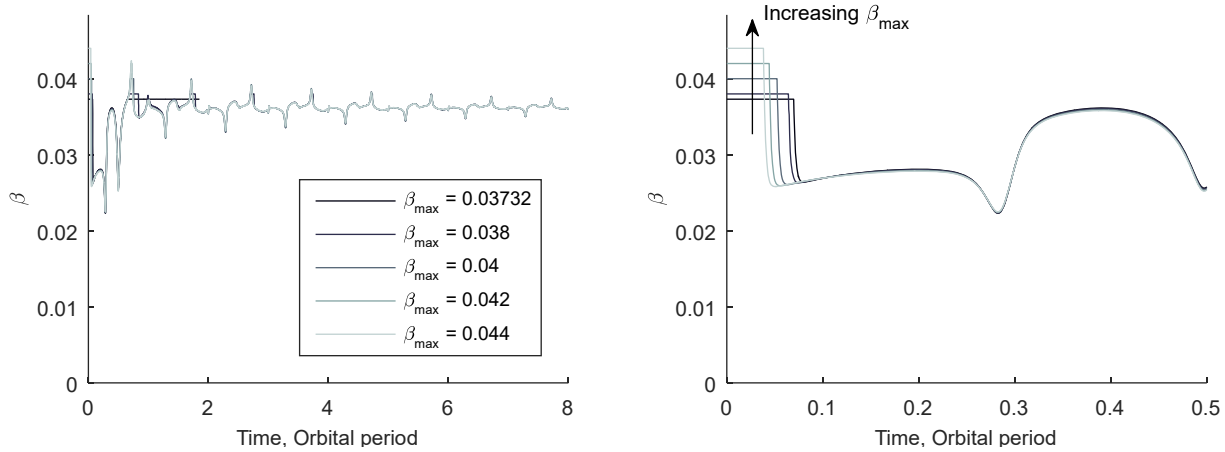

a)

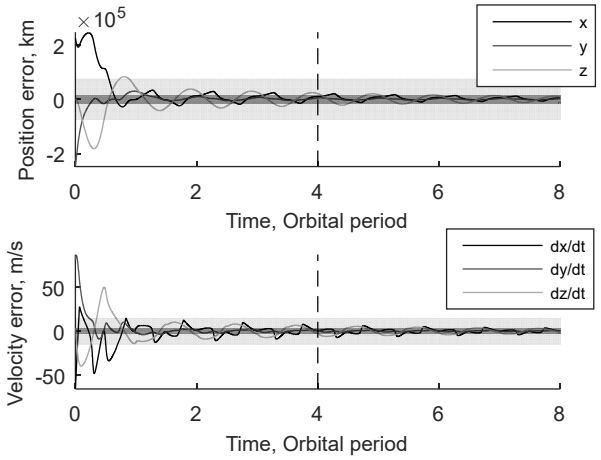

b)

Figure 18 Details for case 1 in Figure 12 (Δr_0 = -500,000 km and $\Delta \dot{r}_0$ = 140 m/s) for different values for β_{max}. a) Lightness number profiles. b) State error profile for β_{max} = 0.038.

1. Additional halo orbits

The results in Figure 12 and Figure 17 have been generated for halo orbits with a nominal lightness number of $\beta_{nom} = 0.0363$. This section investigates the heliogyro performance for some of the other orbits shown in Figure 8, in particular for $\beta_{nom} = 0.01$, 0.02, 0.03, and 0.04. The results are provided in Figure 19, which shows (where possible) the recoverable injection error for both an FPF sail and for a heliogyro, where different values for β_{max} are considered for the heliogyro configuration. In particular, β_{max} is increased with increments of 10% up to an increase of 100%, i.e., $\beta_{max} = \left[1 + \left(i/10\right)\right]\beta_{nom}$ with $i = 1, 2, ..., 10$. Note that for $\beta_{nom} =$ 0.01 and an FPF sail configuration, the recoverable injection error is so small that it is not visible in Figure 19.

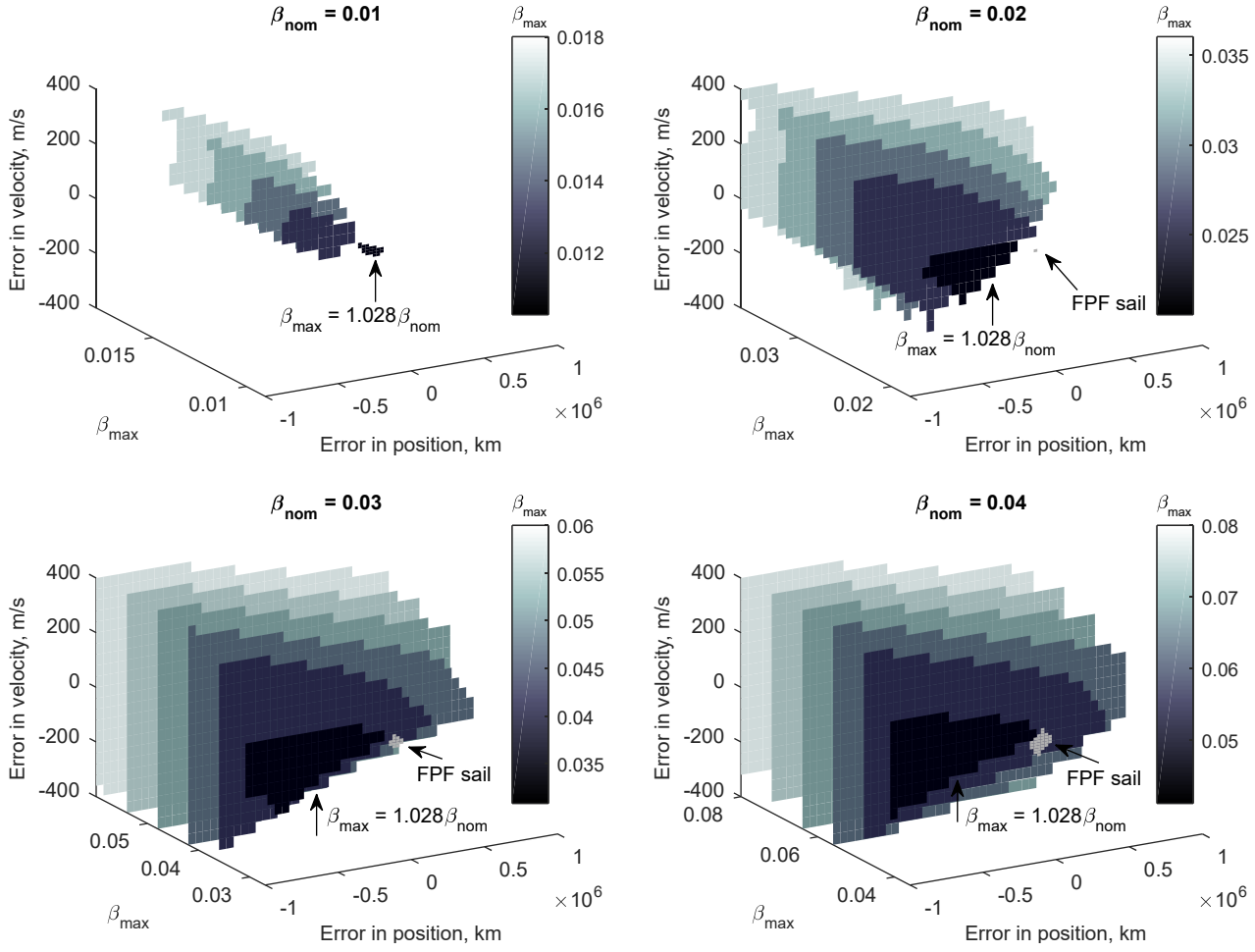

Figure 19 Orbital control of solar sail halo orbits with β_{nom} = 0.01, 0.02, 0.03, and 0.04. Recoverable injection error for FPF sail (only visible for β_{nom} = 0.02, 0.03, and 0.04) and heliogyro for different values for β_{max}.

The results in Figure 19 show that the heliogyro outperforms the FPF sail configuration for all halo orbits considered, with increasing performances for increasing values for β_{max}. Comparing the performance among the different orbits, it becomes clear that the smaller β_{nom}, the smaller the recoverable injection error. This holds both for the heliogyro and the FPF sail configurations, but the orbital control capabilities of the FPF sail degrade faster with decreasing values for β_{nom} than those of the heliogyro.

2. Injection location

The results in this paper thus far have only considered orbit injection at the most northern location of the solar sail halo orbit, i.e., at $y = 0$ and $z > 0$; however, injection may occur at any location along the orbit. In this section, four injection locations, coinciding with the crossings of the (x, z)- and (x, y)-planes, are considered (see Figure 20):

$$\mathbf{r}_{C,0} \rightarrow \begin{cases} y = 0,\ z > 0 & \text{North} \\ z = 0,\ y > 0 & \text{East} \\ y = 0,\ z < 0 & \text{South} \\ z = 0,\ y < 0 & \text{West} \end{cases}. \tag{22}$$

The results are presented in Figure 21 for an FPF sail (subplot a) and for a heliogyro with three different values for β_{max} (subplots b-d). It is clear that the injection location can have a significant influence on the performance of the control, with the 'east' and 'south' locations appearing to perform worst. In addition to the recommendation of injecting slightly Earthward (as concluded at the start of Section VI.A), it can thus be recommended to inject at the 'north' or 'west' locations. However, the larger the value for β_{max} the smaller the influence of the location becomes, with only some minor differences observable at the extremes of the position and velocity error intervals for $\beta_{max} = 0.04$.

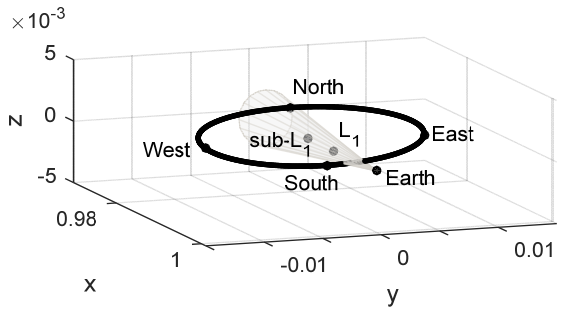

Figure 20 Alternative injection locations along the solar sail halo orbit with β_{nom} = 0.0363.

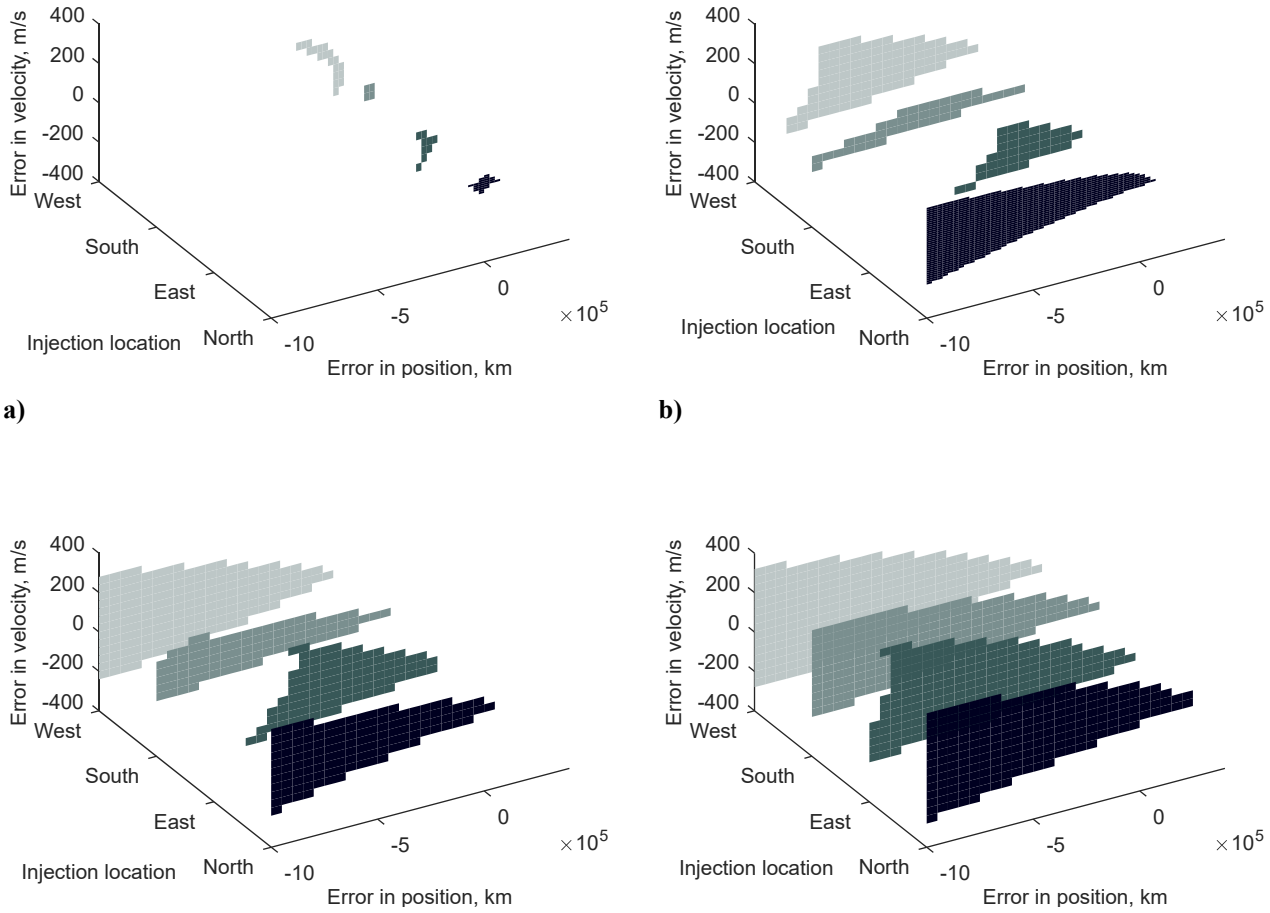

Figure 21 Recoverable injection error for different injection locations along solar sail halo orbit with β_{nom} = 0.0363. a) FPF sail. b-d) Heliogyro with (b) β_{max} = 0.03732, (c) β_{max} = 0.038, and (d) β_{max} = 0.04.

B. Solar sail deployment delay

Next, the case of a delay in solar sail deployment due to deployment failure at injection is considered, starting again with a lightness number equal to that of Sunjammer, i.e., $\beta_{nom} = 0.0363$, as seen in Figure 22. Subplot a) shows the maximum delay in solar sail deployment from which the nominal orbit can still be recovered for a range of β_{max} values. This delay ranges from 1.0 to 7.4 days. For a value of $\beta_{max} = (1 + 0.028)\beta_{nom} = 0.03732$ the results for both an FPF sail and a heliogyro are provided, which show that the FPF sail and heliogyro perform equally well; both allow a delay in sail deployment of one day. To understand these results, details of the three cases numbered one to three in the inset of Figure 22a are provided in Figure 22c-h. When increasing the sail deployment beyond one day (case 1: $\Delta t_0 = 1.1$ days), the trajectory diverges from the solar sail halo orbit (see Figure 22c,d). The LQR controller requests the maximum lightness number, but this is not enough to bring the solar sail back to the halo orbit. This can only be achieved by increasing the maximum value on the lightness number as shown in Figure 22a. Successful control is achieved for both cases 2 and 3 ($\Delta t_0 = 1.0$ and 0.9 days), which both demand heliogyro lightness number profiles that remain almost entirely above the FPF sail's minimum lightness number, β_{min}. The heliogyro's capability to fully scale down the lightness number further than that is thus not used in these cases. As a result, the lightness number profiles for both the heliogyro and the FPF sail configurations are very similar, hence both configurations perform equally well.

The sharp transition between successful control (case 2) and unsuccessful control (case 1) is similar to the bifurcation shown for injection errors in Figure 14. Also, while the final state errors for cases 2 and 3 are smaller than both the loose error tolerance of $\varepsilon = 5 \times 10^{-4}$ and the tight tolerance of $\varepsilon = 10^{-4}$, this is not the case for all time delays and values for β_{max}. Therefore, Figure 22b is included which clearly shows how the definition of successful control changes when changing the error tolerance and for which value of the solar sail deployment delay the control bifurcates to unstable.

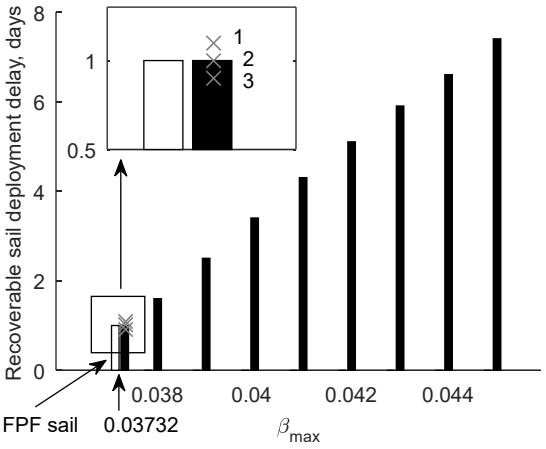
Recoverable sail deployment delay, days
1
2
3
FPF sail
0.03732
0.038
0.04
0.042
0.044
β_{max}

a)

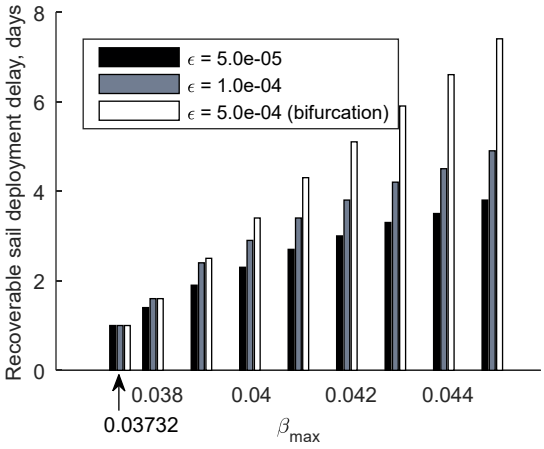
Recoverable sail deployment delay, days
ϵ = 5.0e-05
ϵ = 1.0e-04
ϵ = 5.0e-04 (bifurcation)
0.03732
0.038
0.04
0.042
0.044
β_{max}

b)

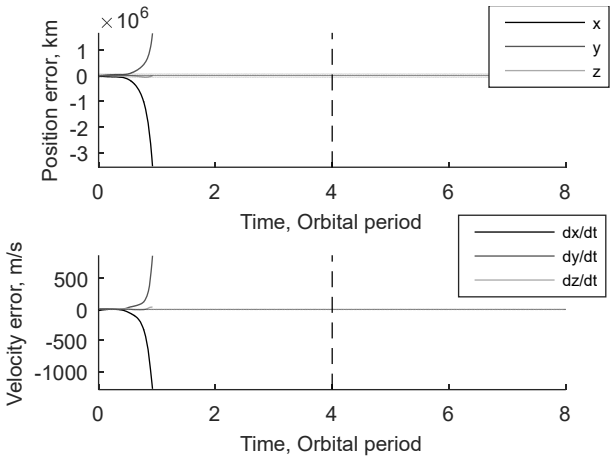
Position error, km
x
y
z
Time, Orbital period
Velocity error, m/s
dx/dt
dy/dt
dz/dt
Time, Orbital period

c)

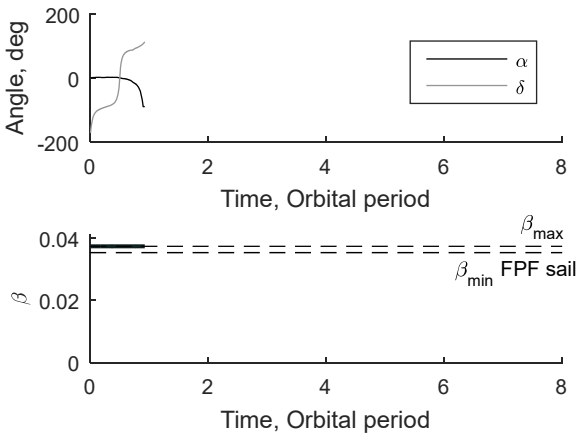
Angle, deg
α
δ
Time, Orbital period
β_{max}
β_{min}
FPF sail
β
Time, Orbital period

d)

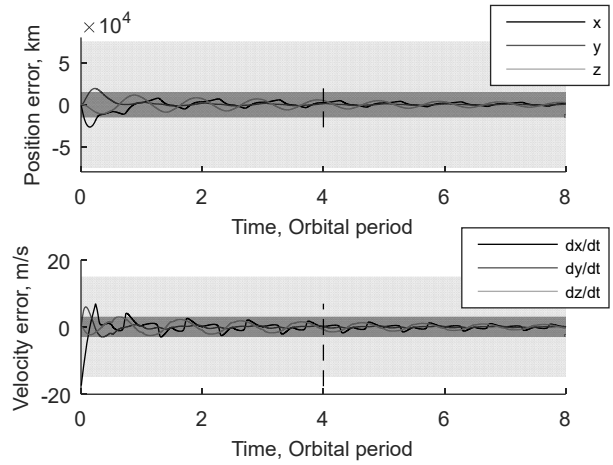
Position error, km
x
y
z
Time, Orbital period
Velocity error, m/s
dx/dt
dy/dt
dz/dt
Time, Orbital period

e)

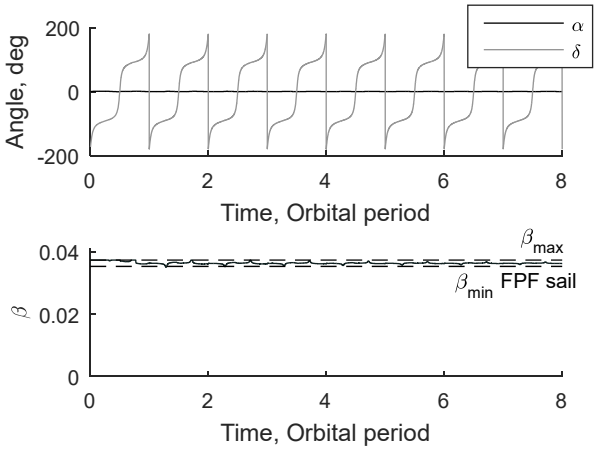
Angle, deg
α
δ
Time, Orbital period
β_{max}
β_{min}
FPF sail
β
Time, Orbital period

f)

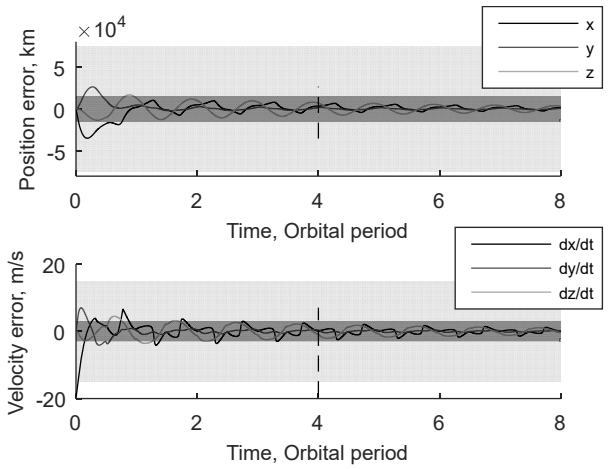

g)

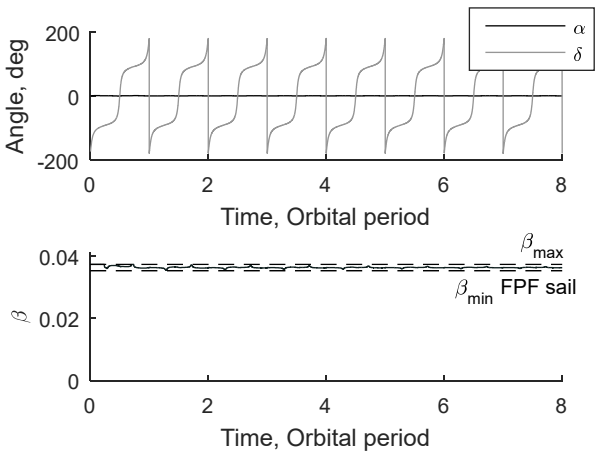

h)

Figure 22 Orbital control of solar sail halo orbit with β_{nom} = 0.0363. a) Recoverable time delay in solar sail deployment after injection for a range of β_{max}-values. b) Influence of error tolerance. c-h) Details of case 1 (c-d), case 2 (e-f), and case 3 (g-h).

The results for the other solar sail halo orbits with $\beta = 0.01,\ 0.02, 0.03$ and 0.04 are presented Figure 23. This figure again shows that the heliogyro's performance increases for larger values for β_{max}. Interestingly, for the same ratio of $\beta_{max} / \beta \geq 1.3$ the solar sail halo orbits with smaller lightness numbers seem to perform better, i.e., allow a larger delay in solar sail deployment than the solar sail halo orbits for larger lightness numbers. This is due to the fact that the same delay in deployment leads to a larger error on the position and velocity at sail deployment for the orbits with a large lightness number, i.e., the classical dynamics deviate more from the solar sail dynamics for large β. This is further illustrated and verified in Figure 24, which shows the error on the state vector at sail deployment in position and velocity for the largest recoverable delay in solar sail deployment for the cases considered in Figure 23. Figure 24 shows that the recoverable deployment delay *time* is relatively small for larger lightness numbers, but the recoverable error in *position* and *velocity* (especially velocity) is much larger. Some final conclusions to be drawn from Figure 23 are that, similar to the results for β_{nom} = 0.0363 in Figure 22a, the FPF sail configuration and the heliogyro with $\beta_{max} = (1 + 0.028)\beta_{nom}$ perform equally well and that the maximum time delay that can be recovered from among all cases considered is 20.2 days.

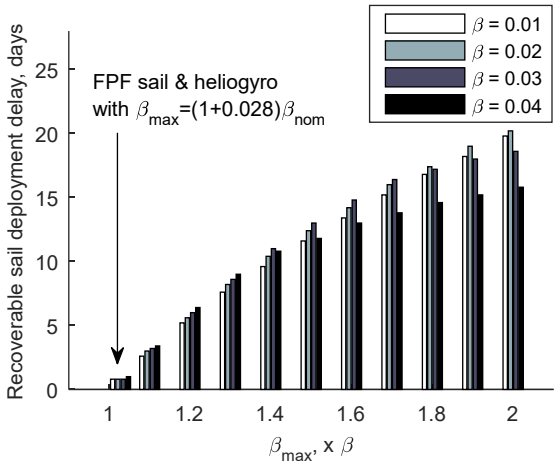

Figure 23 Orbital control of solar sail halo orbits with β_{nom} = 0.01, 0.02, 0.03, and 0.04.

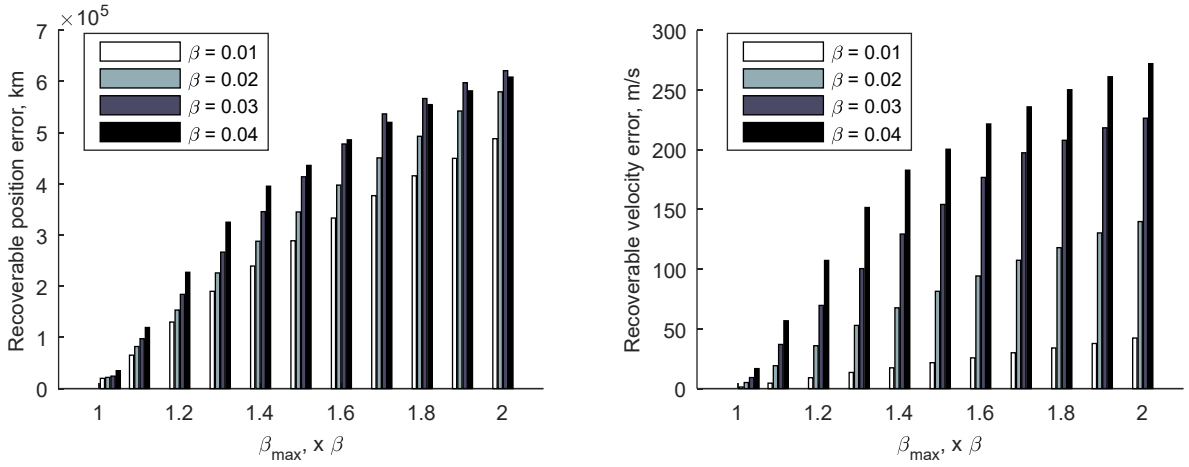

Figure 24 Position and velocity error for maximum recoverable Δt_0 (see Figure 22) for solar sail halo orbits with β = 0.01-0.04 and for a range of β_{max}.

Finally, similar to the sensitivity analysis in Section VII.A, Figure 25 provides an insight in the effect of the injection location on the performance of an FPF sail and that of a heliogyro for recovering from a solar sail deployment failure at injection. Again, for every injection location the FPF sail's performance is the same as that of a heliogyro with $\beta_{max} = (1 + 0.028)\beta_{nom}$. Furthermore, similar to the results for an injection error in Figure 21, the 'east' location performs worst and the influence of the location becomes smaller for larger β_{max} when computing the percentage increase or decrease in allowable sail deployment delay between the injection locations.

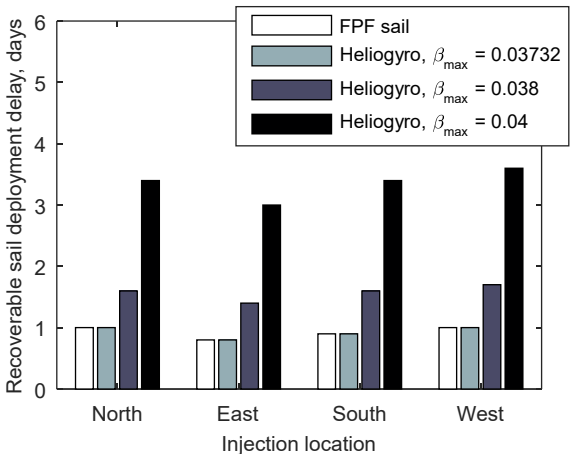

Figure 25 Recoverable time delay in solar sail deployment after injection at different injection locations into solar sail halo orbit with β_{nom} = 0.0363.

VIII. Conclusions

This paper has demonstrated the superior capabilities of a heliogyro for halo-orbit control compared to the traditional fixed polygonal flat (FPF) sail configuration. For a solar sail, Sun-Earth, sub-L_1 halo orbit with a nominal lightness number of $\beta_{nom} = 0.0363$ (technology designed for the previously-proposed Sunjammer mission) and a maximum sail lightness number equal to that of an FPF sail configuration with vanes ($\beta_{max} = 1.028\beta_{nom}$) the heliogyro can accommodate approximately an order of magnitude larger range on the injection position and velocity error than an FPF solar sail. This improved performance is solely due to the heliogyro's capability of fully scaling down the lightness number to zero. A clear bifurcation between stable and unstable control can be established where increasing the tolerance on the residual error in position and velocity after a set amount of time does not provide improvements in performance. Because the control performs better for injection errors Earthward of the nominal injection point than Sunward, it is recommended for operations to undershoot, i.e., intentionally inject slightly Earthward.

When using a larger upper value for the heliogyro's lightness number, β_{max}, even larger injection errors can be recovered. For solar sail halo orbits with other nominal lightness numbers it is shown that the recoverable injection errors scale with β_{nom} for both the heliogyro and the FPF sail, but the heliogyro's recoverable error region is always larger. Finally, considering different injection locations along the orbit, it appears that the injection location has only

a minor effect on the heliogyro's performance for large values for β_{max}, but can significantly deteriorate the performance for 'east' and 'south' injection locations for smaller β_{max}. In that case, injection in the 'north' or 'west' locations is recommended.

When considering a delay in the solar sail deployment past the nominal injection into the solar sail halo orbit, a delay in deployment of 1.0 to 7.4 days can be overcome by both the FPF sail and the heliogyro (with $\beta_{max} = 1.028\beta_{nom}$). Here, the heliogyro's capability of fully scaling down the lightness number does not provide any additional benefit. However, larger values for β_{max} do provide better performance, up to a maximum value of 20.2 days among all solar sail halo orbits considered. Finally, the effect of the injection location is only small for the case of a sail deployment delay and the error tolerance has a similar effect as established for the case of an injection error with a clear bifurcation between stable and unstable control.

Appendix

To transform between the reference frames of Figure 1, the following rotation operations are required, where the following definition and notation of the standard rotation matrices is adopted:

$$R_{x,\vartheta} = \begin{bmatrix} 1 & 0 & 0 \\ 0 & \cos\vartheta & -\sin\vartheta \\ 0 & \sin\vartheta & \cos\vartheta \end{bmatrix}, \; R_{y,\vartheta} = \begin{bmatrix} \cos\vartheta & 0 & \sin\vartheta \\ 0 & 1 & 0 \\ -\sin\vartheta & 0 & \cos\vartheta \end{bmatrix}, \; R_{z,\vartheta} = \begin{bmatrix} \cos\vartheta & -\sin\vartheta & 0 \\ \sin\vartheta & \cos\vartheta & 0 \\ 0 & 0 & 1 \end{bmatrix}. \tag{23}$$

1. Transformation from $D\left(\hat{\mathbf{d}}_1, \hat{\mathbf{d}}_2, \hat{\mathbf{d}}_3\right) \rightarrow S\left(\hat{\mathbf{s}}, \hat{\mathbf{l}}, \hat{\mathbf{p}}\right)$

   A vector in, $D\left(\hat{\mathbf{d}}_1, \hat{\mathbf{d}}_2, \hat{\mathbf{d}}_3\right)$, $\mathbf{x}_D$, can be transformed to a vector in $S\left(\hat{\mathbf{s}}, \hat{\mathbf{l}}, \hat{\mathbf{p}}\right)$, $\mathbf{x}_S$, through

$$\mathbf{x}_S = R_{x,\gamma} R_{z,\eta} \mathbf{x}_D = [SD]\mathbf{x}_D \tag{24}$$

2. Transformation from $B\left(\hat{\mathbf{b}}_1, \hat{\mathbf{b}}_2, \hat{\mathbf{b}}_3\right) \rightarrow D\left(\hat{\mathbf{d}}_1, \hat{\mathbf{d}}_2, \hat{\mathbf{d}}_3\right)$

   A vector in $B\left(\hat{\mathbf{b}}_1, \hat{\mathbf{b}}_2, \hat{\mathbf{b}}_3\right)$, $\mathbf{x}_B$, can be transformed to a vector in $D\left(\hat{\mathbf{d}}_1, \hat{\mathbf{d}}_2, \hat{\mathbf{d}}_3\right)$, $\mathbf{x}_D$, through

$$\mathbf{x}_D = R_{y,-\frac{\pi}{2}} R_{x,\pi} R_{z,\psi_1} \mathbf{x}_B = [DB]\mathbf{x}_B, \tag{25}$$

   where ψ_i is defined as

$$\psi_i = \Omega t + \chi_i, \quad \chi_i = 2\pi \frac{i-1}{N}, \tag{26}$$

with i the i^{th} blade number, Ω the heliogyro spin rate, and N the number of heliogyro blades. The constant π and $-\pi/2$ rotations are merely to change the axis numbering to align with convention in literature.

3. Transformation from $L_i\left(\hat{\mathbf{l}}_1,\hat{\mathbf{l}}_2,\hat{\mathbf{l}}_3\right) \rightarrow B\left(\hat{\mathbf{b}}_1,\hat{\mathbf{b}}_2,\hat{\mathbf{b}}_3\right)$

   A vector in $L_i\left(\hat{\mathbf{l}}_1,\hat{\mathbf{l}}_2,\hat{\mathbf{l}}_3\right)$, $\mathbf{x}_{L_i}$, can be transformed to a vector in $B\left(\hat{\mathbf{b}}_1,\hat{\mathbf{b}}_2,\hat{\mathbf{b}}_3\right)$, $\mathbf{x}_B$, through

$$\mathbf{x}_B = R_{z,\chi_i} R_{x,\theta_i} \mathbf{x}_{L_i} = \left[BL_i\right]\mathbf{x}_{L_i}, \tag{27}$$

   with θ_i the pitch angle of the blade.

Acknowledgments

Jeannette Heiligers would like to acknowledge the support of the John Moyes Lessells Travel Scholarship of the Royal Society of Edinburgh and the Marie Skłodowska-Curie Individual Fellowship 658645 - S4ILS: Solar Sailing for Space Situational Awareness in the Lunar System.

References

1. McInnes, C.R., "Solar Sailing: Technology, Dynamics and Mission Applications," *Springer-Praxis Books in Astronautical Engineering*, Springer-Verlag, Berlin, 1999.
2. Vulpetti, G., Johnson, L., and Matloff, G.L., "Solar Sails A Novel Approach to Interplanetary Travel, 2nd Edition," *Springer-Praxis Books in Space Exploration*, 2nd ed., Springer Science+Business Media, New York, 2015.
3. Tsuda, Y., Mori, O., Funase, R., Sawada, H., Yamamoto, T., Saiki, T., Endo, T., Yonekura, K., Hoshino, H., and Kawahuchi, J., "Achievement of IKAROS - Japanese deep space solar sail demonstration mission," *Acta Astronautica*; Vol. 82, 2013, pp. 183-188. doi: 10.1016/j.actaastro.2012.03.032
4. Johnson, L., Whorton, M., Heaton, A., Pinson, R., Laue, G., and Adams, C., "NanoSail-D: A Solar Sail Demonstration Mission," *Acta Astronautica*; Vol. 68, 2011, pp. 571-575. doi: 10.1016/j.actaastro.2010.02.008
5. Wilkie, W.K., Warren, J.E., Guerrant, D.V., Lawrence, D.A., Gibbs, S.C., Dowell, E.H., Heaton, A.F., Juang, J., Horta, L.G., Lyle, K.H., Littell, J.D., Bryant, R.G., Thomson, M.W., and Walkemeyer, P.E., "Heliogyro Solar Sail Research at NASA," *Advances in Solar Sailing*, Springer Praxis-Books - Astronautical Engineering, Berlin, 2013, pp. 631-650.
6. MacNeal, R.H., "Helicopters for Interplanetary Space Flight," *34th National Forum of the American Helicopter Society*, American Helicopter Soc., Washington, D.C., 1978.
7. Guerrant, D. and Lawrence, D., "Nonlinear Torsional Dynamics and Control of Heliogyro Solar Sail Blades (AIAA 2015-0435)," *2nd AIAA Spacecraft Structures Conference*, Reston, Virginia, USA, 2015.
8. Guerrant, D. and Lawrence, D., "Tactics for Heliogyro Solar Sail Attitude Control Via Blade Pitching," *Journal of Guidance, Control, and Dynamics*; Vol. 38, 2015, pp. 1785-1799. doi: 10.2514/1.G000861
9. McMahon, J.W. and Lawrence, D.A., "Orbital Maneuvering with a Solar Sail through the Use of Natural Attitude Coning," *Advances in the Astronautical Sciences*; Vol. 135, 2009, pp. 713-726
10. West, J.L., "The GeoStorm Warning Mission: Enhanced Opportunities Based on New Technology," *14th AAS/AIAA Spaceflight Mechanics Conference*, AAS-04-102, Maui, Hawaii, 2004.

11. Heiligers, J., Diedrich, B., Derbes, B., and McInnes, C.R., "Sunjammer: Preliminary End-to-End Mission Design," *2014 AIAA/AAS Astrodynamics Specialist Conference*, San Diego, CA, USA, 2014.
12. Macdonald, M. and McInnes, C.R., "Solar Sail Mission Applications and Future Advancement," *2nd International Symposium on Solar Sailing*, New York, New York, 2010.
13. Lawrence, D. and Piggott, S., "Integrated Trajectory and Attitude Control for a Four-Vane Solar Sail (AIAA 2005-6082)," *AIAA Guidance, Navigation, and Control Conference*, San Francisco, California, USA, 2005.
14. Lawrence, D. and Piggott, S., "Solar Sailing Trajectory Control for Sub-L1 Stationkeeping (AIAA 2004-5014)," *AIAA Guidance, Navigation and Control Conference*, Providence, Rhode Island, USA, 2004.
15. Church, E.L. and Takacs, P.Z., "Surface Scattering," *Handbook of Optics*, 3 ed., Vol. I, McGraw Hill, New York, USA, 2010.
16. Stover, J.C., "Optical Scattering - Measurement and Analysis," 3 ed., SPIE Press, Washington, 2012.
17. Vulpetti, G., "Applying Vector Scattering Theory to Solar-Photon Sail Thrust Modeling," *Advances in Solar Sailing*, Springer, 2014.
18. Guerrant, D. and Lawrence, D., "Heliogyro Attitude Control Moment Authority via Blade Pitch Maneuvers," *Advances in Solar Sailing*, Springer Praxis-Books - Astronautical Engineering, Berlin, 2014, pp. 667-686.
19. MacNeal, R.H., "Structural Dynamics of the Heliogyro," National Aeronautics and Space Administration, NASA CR-17445A, Washington, D.C., 1971.
20. Eldad, O. and Lightsey, E.G., "Attitude Control of the Sunjammer Solar Sail Mission," *28th Annual AIAA USU Conference on Small Satellites*, Logan, Utah, USA, 2014.
21. Goddard Space Flight Center, "Advanced Composition Explorer ACE - Detailed Mission Requirements," National Aeronautics and Space Administration, GSFC-410-ACE-017, 1995.
22. McInnes, A.I.S., "Strategies for Solar Sail Mission Design in the Circular Restricted Three-Body Problem," M.S. Dissertation, Purdue University, School of Aeronautics and Astronautics, West Lafayette, 2000.
23. Nuss, J.S., "The Use of Solar Sails in the Circular Restricted Problem of Three Bodies," M.S. Dissertation, Purdue University, West Lafayette, 1998.
24. Baoyin, H. and McInnes, C., "Solar Sail Halo Orbits at the Sun-Earth Artificial L1-point," *Celestial Mechanics and Dynamical Astronomy*; Vol. 94, 2006, pp. 155-171. doi: 10.1007/s10569-005-4626-3
25. Battin, R.H., "An Introduction to the Mathematics and Methods of Astrodynamics, Revised Edition," *AIAA Eduction Series*, American Institute of Aeronautics and Astronautics, Inc., Reston, USA, 1999.
26. Wawrzyniak, G.G. and Howell, K.C., "Numerical Techniques for Generating and Refining Solar Sail Trajectories," *Advances in Space research*; Vol. 48, 2011, pp. 1848-1857. doi: 10.1016/j.asr.2011.04.012
27. Waters, T.J. and McInnes, C.R., "Periodic Orbits Above the Ecliptic in the Solar-Sail Restricted Three-Body Problem," *Journal of Guidance, Control, and Dynamics*; Vol. 30, No. 3, 2007, pp. 687-693. doi: 10.2514/1.26232
28. Heiligers, J., Hiddink, S., Noomen, R., and McInnes, C.R., "Solar Sail Lyapunov and Halo Orbits in the Earth-Moon Three-Body Problem," *Acta Astronautica*; Vol. 116, 2015, pp. 25-35. doi: 10.1016/j.actaastro.2015.05.034
29. Ceriotti, M. and McInnes, C.R., "Hybrid Solar Sail and SEP Propulsion for Novel Earth Observation Missions," *61st International Astronautical Congress*, Prague, Czech Republic, 2010.
30. Heiligers, J., Ceriotti, M., McInnes, C.R., and Biggs, J.D., "Design of Optimal Transfers Between North and South Pole-Sitter Orbits," *22nd AAS/AIAA Space Flight Mechanics Meeting*, Charleston, SC, 2012.
31. Ceriotti, M., Heiligers, J., and McInnes, C.R., "Trajectory and Spacecraft Design for a Pole-Sitter Mission," *Journal of Spacecraft and Rockets*; Vol. 51, No. 1, 2014, pp. 311-326. doi: 10.2514/1.A32477